Reprint from *Turbulence Structure and Modulation*, Eds. Soldati, A., and Monti, R., Springer-Verlag, Wien, pp. 119-160 (2001).

Prospects for Modulation of Turbulent Boundary Layer by EHD Flows

Alfredo Soldati* and Cristian Marchioli

Centro di Fluidodinamica e Idraulica and Dipartimento di Scienze e Tecnologie Chimiche, University of Udine, 33100, Udine, Italy

Abstract. In this paper, we present a review of the recent results obtained in the field of boundary layer modification using large-scale ElectroHydroDynamic (EHD) flows. EHD flows are a characteristic of Electrostatic Precipitators (ESPs) and the study of their interactions with the turbulent boundary layer may lead to optimization of ESPs from the viewpoint of drag reduction and particle collection efficiency. However, this study has a general relevance since EHD flows may be exploited in a number of industrial applications to modulate turbulence. In this work, we describe the principles of turbulence structure at the wall and then present results obtained for turbulent boundary layer forced by different configurations of EHD flows. Finally, we describe possible improvements and the optimization of the method.

1 Introduction

Turbulence modulation in the boundary layer is important for a number of applications ranging from drag reduction to control heat or mass transfer at the wall in various devices of the process industry. Turbulence modulation is based on introducing some sort of perturbation into the flow field which can affect the dynamics of turbulence structure at the wall, and, so, turbulent transfer mechanisms. Specifically, this perturbation may be superimposed onto the flow either by modifying the boundary conditions or by some sort of body force acting directly on the fluid parcels. In this work, we will consider the influence of a steady electric body force acting directly on the fluid. In particular, we will consider a fluid with dispersed ionic species forced by an external electrostatic field. This phenomenon is common in Electrostatic Precipitators (ESP) (Yamamoto and Velkoff, 1981, Leonard et al., 1983, Kallio and Stock, 1992, Soldati and Banerjee, 1998, Soldati, 2000a) but the study of the interaction of electrostatic body forces and turbulent flows has relevance in a number of other applications, ranging from aerospace technology (Malik et al., 1983, Massines et al., 1998, Roth et al., 1998, Roth et al., 2000) to heat transfer technology (Velkoff and Godfrey, 1979, Ohadi et al., 1991, Owsenek et al., 1995, Owsenek et al., 1997) down to surface sterilization (Kelly-Wintenberg et al., 1998, Montie et al., 2000). We will focus on the modification of the turbulent transfer mechanisms which can be exploited in geometries similar to that of Electrostatic Precipitators.

In the most widely used configuration, an ESP is constituted by two vertical grounded plates through which the dust-laden gas flows horizontally. Regularly spaced, vertical thin wires are

* Corresponding author. Email: soldati@uniud.it; Ph.: +390432558864; Facs: +390432558803; www: 158.110.50.22

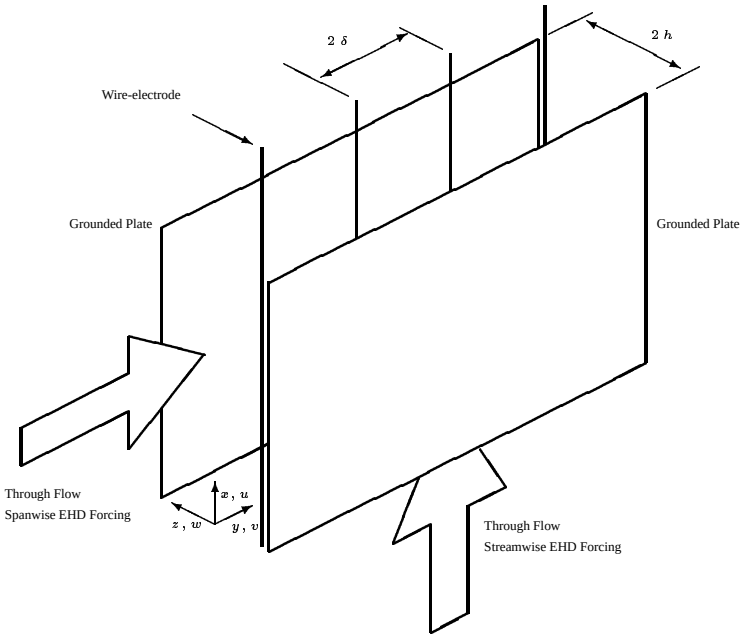

Figure 1. Diagram of wire-plate ESP with proposed new flow configuration. Wires may be also placed onto one wall.

placed in the middle of the duct and are kept at high potential in order to discharge the ions required to charge the initially neutral airborne particles that are to be separated. Under common operating conditions, the ions discharged by the wires are accelerated towards the wall and generate spanwise plane jets which, in turn, produce spanwise two-dimensional vortices of the size of the wire-to-wall distance (Yamamoto and Velkoff, 1981, Kallio and Stock, 1992, Soldati and Banerjee, 1998, Soldati, 2000a). These flows are called ElectroHydroDynamic (EHD) flows. In practice, if ionic discharge occurs uniformly along the wires, and this is usually the case for positive corona discharge, the distribution of the body force is two-dimensional. Thus, depending on the orientation of the flow with respect to the wires, as shown in Figure 1, it is possible to force the boundary layer either with large-scale spanwise vortices – usual operating configuration – or with large-scale streamwise vortices – proposed operating configuration.

A sound understanding of the complex interactions of the EHD flows and the structure of turbulence at the wall might lead to the optimization of turbulent transfer mechanisms at the wall, leading to drag reduction, particle-collection increase and possible control of mass transfer at the wall which could be relevant for new applications of ESPs, such as $NO_{\times}$ control (Dinelli and Rea, 1990, Dinelli et al., 1991). However, in order to identify the optimal geometrical configuration for EHD forcing, a detailed knowledge of the dynamics of turbulence in the boundary layer is required.

In this paper, we review the recent results obtained in our laboratory. First, we describe the characteristics of turbulence in the wall boundary layer. Second, we examine the modifications of

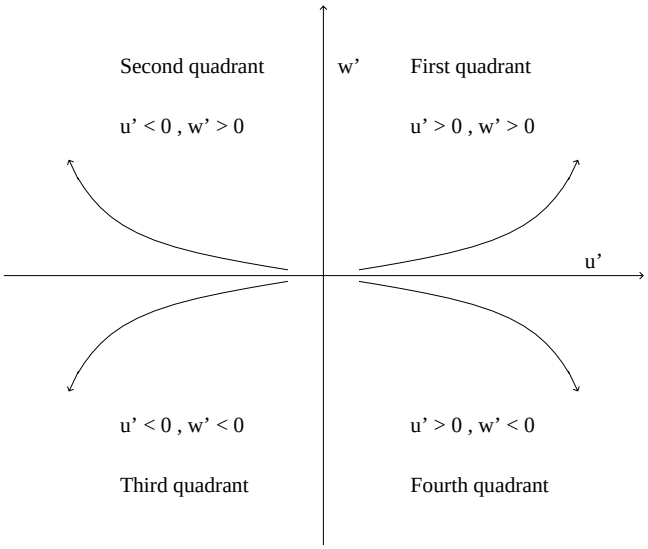

Figure 2. Identifications of $u'w'$ Reynolds stresses: $u' - w'$ plane.

turbulence structure due to the forcing of spanwise EHD vortical flows, i.e. the usual configuration for positive corona ESPs; finally, we consider a possible new configuration for ESPs and we examine the modifications in the structure of the boundary layer due to the action of streamwise vortical flows. Specifically, we were prompted by a recent paper by Schoppa and Hussain (1998), who were able to damp turbulence in channel flow by exploiting large-scale, streamwise independent vortical flows. Hussain and coworkers found (Schoppa and Hussain, 1996, Jeong et al., 1997, Schoppa and Hussain, 1997) that turbulence structures could be stabilized by a appropriate large-scale lateral forcing and superimposed *synthetically* generated streamwise vortical flows −i.e. mathematical functions −onto a turbulent channel flow (Schoppa and Hussain, 1998). We will try to implement their concept from a physical viewpoint by forcing EHD flows onto a turbulent boundary layer.

2 Wall Turbulence Phenomena in a Boundary Layer

We consider in this section the boundary layer which occurs in the fully developed channel flow. The reference geometry is that shown in Figure 1. The mean flow is towards the positive x. In a turbulent boundary layer, momentum, heat and mass transfer are controlled by the Reynolds stresses. Of the convective, correlation events which characterize the Reynolds stresses, strong local motions of fluid which are called *ejections* and *sweeps* are the most efficient transfer agents and control turbulent mixing close to the wall. Specifically, ejections bring the low-momentum fluid close to the wall into the outer region whereas sweeps bring the high-momentum fluid from the outer flow into the wall region. Ejections and sweeps control momentum transfer at the wall

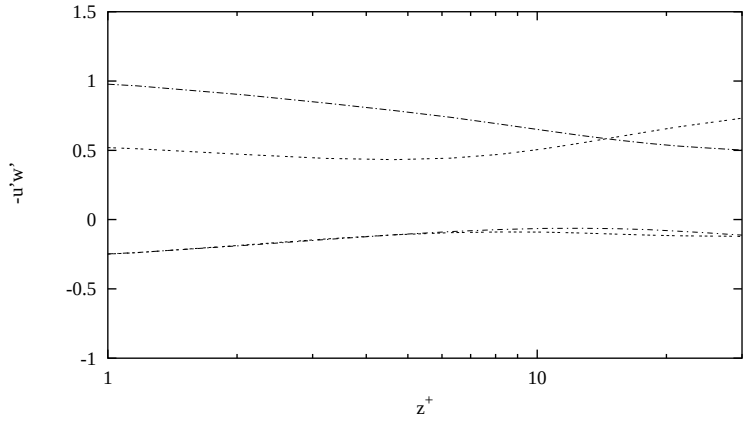

Figure 3. Quadrant analysis of $u'w'$.

and are also well correlated to heat transfer (Papavassiliou and Hanratty, 1995, Kasagi and Iida, 1998) and mass transfer (De Angelis et al., 1996) at the wall. A complete characterization of sweeps and ejections and of their generation mechanisms is thus fundamental in order to gain insight into the physics of turbulence structure at the wall. In the next section, we will characterize first turbulence events in the wall layer from a statistical viewpoint, and then we will describe the dynamics of the wall structures which control the Reynolds stresses. We will exploit our DNS database for channel flow computed in Soldati et al. (1993). The DNS database is relative to a pseudo-spectral DNS calculation of a closed channel flow at a shear Reynolds number of 108 [1].

2.1 Statistics of Turbulence Phenomena at the Wall

Reynolds stresses may be conveniently examined by employing the quadrant analysis for the wall-normal (w') and the streamwise (u') component of the fluctuating velocity field (Willmarth and Lu, 1972). Considering the events in the $u' - w'$ plane shown in Figure 2, the drag generating events fall in the second and in the fourth quadrant. Both these type of events contribute to the negative Reynolds stresses, i.e. to positive turbulence production, thus their increase corresponds in general to an increase in drag. First and third quadrant events contribute to positive Reynolds stress, i.e. to negative turbulence production and their increase corresponds in general to a decrease in drag. Second quadrant events are called *ejections* and correspond to jets of low streamwise momentum directed outward. Fourth quadrant events are called *sweeps* and correspond to jets of high streamwise momentum directed toward the wall. As in previous DNS works (Kim et al., 1987), we performed the quadrant analysis in the case of a plane boundary layer by

[1] The shear Reynolds number is $Re_\tau = u_\tau h/\nu$, where u_τ is the shear velocity and ν is kinematic viscosity. The shear velocity is defined as:

$$u_\tau = \sqrt{\frac{\tau_w}{\rho}} \tag{1}$$

where τ_w is the wall shear stress and ρ is the fluid density.

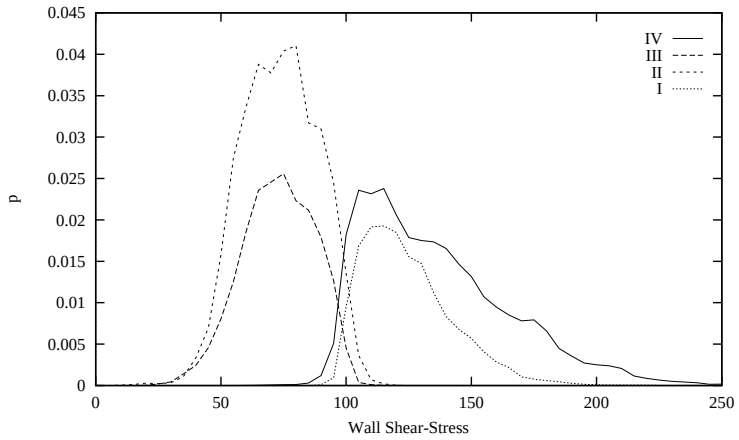

Figure 4. Probability function of coherent $u'w'$ events versus wall shear stress.

time-averaging and space-averaging over the $x - y$ plane the mean fractional contribution to the Reynolds stress from each quadrant. Results are shown in Figure 3, plotted as a function of the wall distance, z^+, and normalized by the mean value of $u'w'$ at the wall distance considered. Very close to the wall, the sweep events (quadrant IV) predominate over the ejection events (quadrant II). In other words, the fraction of the Reynolds stress associated with the sweep event is larger than that associated with the ejection event. Farther from the wall, ejection events dominate, with a crossover point at $z^+ \simeq 12$.

In order to examine the spatial relationship of the different events and the shear stress at the wall, we calculated the probability distributions of first, second, third and fourth quadrant events as functions of the shear stress at the wall. We followed the procedure used by Lombardi et al. (1996) and we considered only those events with significant spatial coherence. The probability density functions are shown in Figure 4. Sweeps and ejections are separated by the level of wall shear stress they generate: sweeps clearly correspond to high shear stress region, whereas ejections correspond to regions of low shear stress. Considering that the average value of the shear stress at the wall is 108, about 86% of the sweeps correspond to value of the shear stress above the average, whereas 98% of the ejections induce shear stress values lower than the average.

2.2 Dynamics of Turbulence Structures at the Wall

In the previous section, we examined the statistical relationship between the Reynolds stress and the shear stress at the wall. We will try to visualize the single events and the dynamics of the structures which control their occurrence. The correlations "sweep-high shear stress" and "ejection-low shear stress" demonstrated in Figure 4, may be appreciated in the snapshot shown in Figure 5, where the footprint of the shear-stress at the wall is shown together with sweep and ejection events. In this figure, sweeps and ejections are identified with the same isocontour of the instantaneous surface at $u'w' = -3$ in wall units. As discussed before, low shear-stress regions,

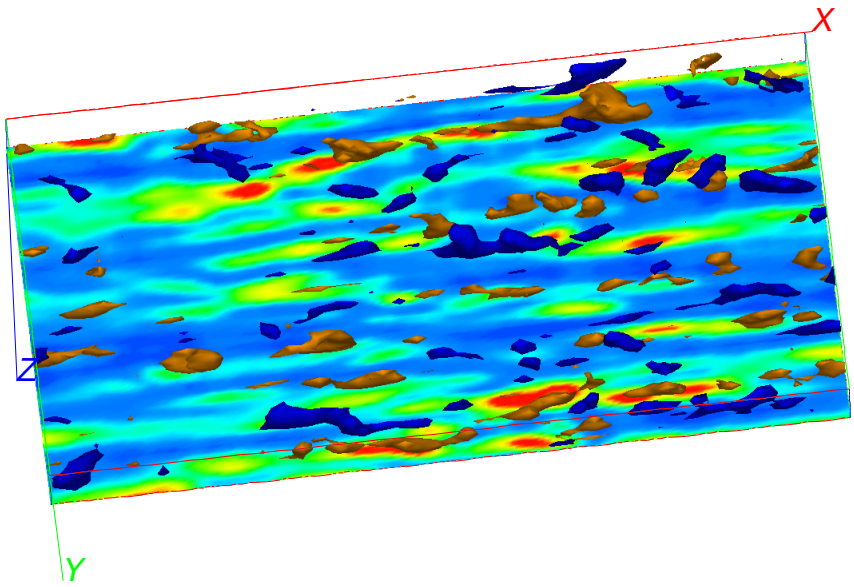

Figure 5. Snapshot footprint of the wall shear-stress with corresponding sweep and ejection events in the whole computational domain. At the wall, red indicates high shear-stress; blue indicates low shear-stress. Gold 3D regions are isosurfaces characterizing sweeps whereas blue 3D regions characterize ejections. 3D isosurfaces are traced at $u'w' = -3$ in dimensionless units. A time-sequence animation of the events shown in this Figure may be retrieved at `http://158.110.50.22/turbulent/movie1.htm`

shown in blue, correspond to the ejections (blue lumps), whereas high shear-stress regions, in red, correspond to the sweeps (gold lumps). Sweeps and ejections are just the final outcome of the dynamics of turbulence structures in the wall layer, and there is still some uncertainty about the mechanisms which generate and maintain the sweep / ejection events. They appear to be generated by the quasi-streamwise vortices which populate the near wall region.

Quasi-streamwise vortices have been the object of a number of works starting with Kline et al. (1967). There is a general agreement about their characteristics, and quasi-streamwise vortices appear to have a characteristic length of about 200 wall units and a spacing of about 400 wall units (Kline and Robinson, 1990, Jeong et al., 1997, Schoppa and Hussain, 1997, Jimenez and Pinelli, 1999). These vortices are slightly tilted away from the wall and are responsible for pumping fluid towards and away from the wall. Quasi-streamwise vortices are slightly tilted upward $-$about 9^o average (Schoppa and Hussain, 1997); clockwise and counterclockwise rotating vortices are also slightly tilted about 4^o left and right respectively. The streamwise vortices may be identified by using pressure (Kasagi and Ohtsubo, 1993), vorticity (Jeong and Hussain, 1995) or other indicators (Bonnet and Delville, 1996, Bonnet et al., 1998, Hunt et al., 1998, Dubief and

Figure 6. Quasi-streamwise counterrotating vortices together with ejections and sweeps. Quasi-streamwise vortices extend for about $200 - 300$ wall units. Two isosurfaces of the same absolute value of Ω indicate clockwise rotating (red) and counterclockwise rotating (pale blue) vortices. Sweeps and ejections are indicated by green and blue respectively. A time-sequence animation of the events shown in this Figure may be retrieved at `http://158.110.50.22/turbulent/movie2.htm`

Delcayre, 2000). A convenient method for identification is based on calculating the eigenvalues of the strain rate tensor Ω (Perry and Chong, 1987, Chong et al., 1990, Jeong and Hussain, 1995). The vector Ω is related to the streamline rotation, represents the strength and direction of the rotation of the streamlines, and is associated with the complex eigenvalues of the strain rate tensor. In Figure 6, two counterrotating vortices, identified by one isosurface of Ω, are shown together with the ejections and sweeps they generate. The elongated red and pale blue structures are two isosurfaces with the same absolute value of Ω (and opposite sign) and indicate clockwise rotating (red) and counterclockwise rotating (pale blue) vortices. Flow is going from bottom left to top right in figure and vortices appear tilted away from the wall by the mean strain rate. The blue lumps of fluid in between the two vortices are ejections and the green lumps of fluid outside the two vortices are sweeps. Ejections and sweeps also appear to be affected by the mean strain rate.

Owing to the continuous action of the quasi-streamwise vortices in generating sweeps and ejections, regions between two vortices such as those shown in Figure 6 are characterized by a streamwise velocity lower than the mean, whereas the regions outside the two vortices are characterized by a streamwise velocity higher than the mean. Specifically, the regions with velocity lower than the mean are called low-speed streaks, whereas the regions with velocity higher than the mean are called high-speed regions. Many quasi-streamwise vortices are usually associated

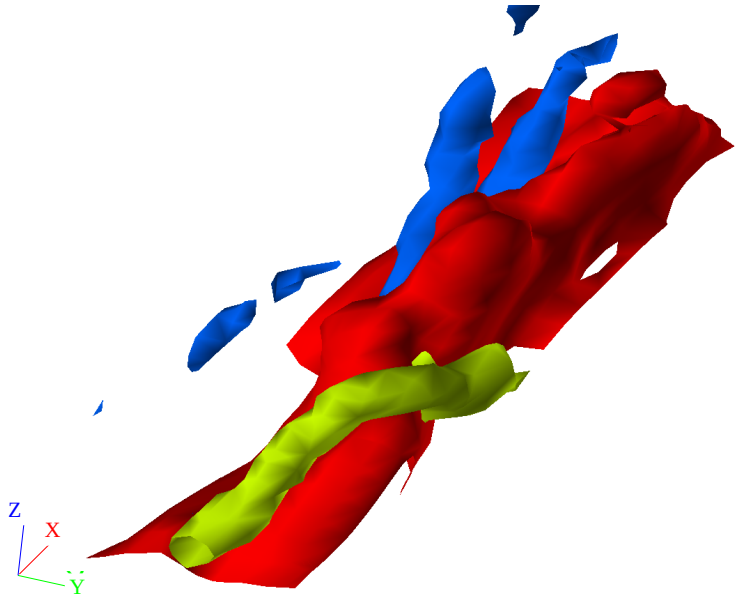

Figure 7. Two counterrotating quasi-streamwise vortices onto a single low-speed streak (red). Green isosurface of Ω indicates clock-wise rotating vortex, blue isosurface of Ω indicates counter clock-wise rotating vortex.

with one single low-speed streak. Low-speed streaks are sinuous regions about 1000 wall units long and are more coherent than the high-speed regions. In Figure 7, a 450 wall units long piece of one low-speed streak is shown, flanked by two counter-rotating quasi-streamwise vortices. In this figure, the action of the quasi-streamwise vortices in lifting up the low-speed streak is clear. Streamwise vortical structures overlap in x as a staggered array, and this is clearly shown in Figure 8, where quasi-streamwise vortices are shown associated with one low-speed streak $-$a 650 wall unit-long piece of one low-speed streak. One single low-speed streak has a longer life than quasi-streamwise vortices and survives a number of vortex generations. In Figure 9, one single low-speed streak is shown for a length of about 1200 wall units. The isosurface indicates a streamwise velocity value of $0.56\ U_c$ where U_c is centerline velocity. The streak is sinuous and, in time, oscillates with a meandering motion in the spanwise direction. The isosurface of the streak has different slope and shape at different locations. It has been shown (Kim and Hussain, 1993) that the generation of the quasi-streamwise vortices is associated with changes in the shape of the low-speed streak surface (Soldati, 2000b). The Lagrangian evolution of the shape of a low-speed streak is shown in Figure 10. The section shown in Figure 10 a) is followed downstream with the velocity $0.56\ U_c$ which is the advection velocity of the low-speed streak (Kim and Hussain, 1993). This enables a Lagrangian tracking of the evolution of the chosen section of the streak. During the sequence shown in Figure 10, the wall layer undergoes a quiescent phase, Figures 10 a) and b), during which there is no evidence of quasi-streamwise vortices, and an active phase, Figure 10 c), d) and e), during which there is an alternate appearance of quasi-

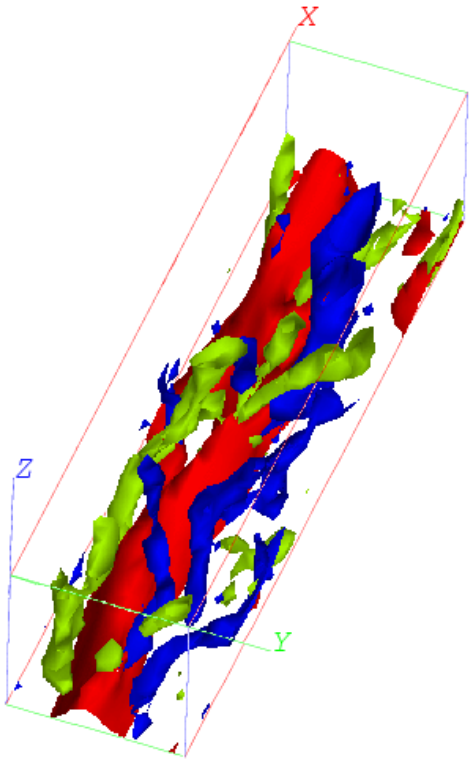

Figure 8. One low-speed streak (red) with counterrotating quasi-streamwise vortices in a box about 150 wall units wide and 650 wall units long. Clockwise rotating vortices (blue) are on the right side of the low-speed streak and are slightly tilted right; counterclockwise rotating vortices (green) are on the left side and are slightly tilted left.

streamwise vortices of opposite sign, and again a quiescent phase, Figure 10 f). It is interesting to observe that clockwise and counterclockwise rotating vortices do not appear at the same time in the same location, as discussed by Schoppa and Hussain (1997). Over the whole cycle, the section of the streak was advected downstream for 640 wall units. It is clear that changes in the shape of the cross section of the low-speed streaks are associated to the occurrence of quasi-streamwise vortices. Since quasi-streamwise vortices control turbulence transfer mechanisms at the wall, the key to control transfer rates is to control quasi-streamwise vortices.

In recent papers, Schoppa and Hussain (1997, 2000) suggested that wall turbulence is dominated by a cycle in which low-speed streaks generate quasi-streamwise vortices, which in turn generate ejections and sweeps. These finally contribute to maintain the low-speed streaks. A crucial question is how the low-speed streaks can generate the quasi-streamwise vortices. Schoppa and Hussain (1997) answer this by examining the behavior of a single low-speed streak and finding that it is subject to lateral, sinuous instability. Stability analysis of an idealized low-speed streak showed it to be unstable to lateral perturbations. Basing their examination also on the DNS

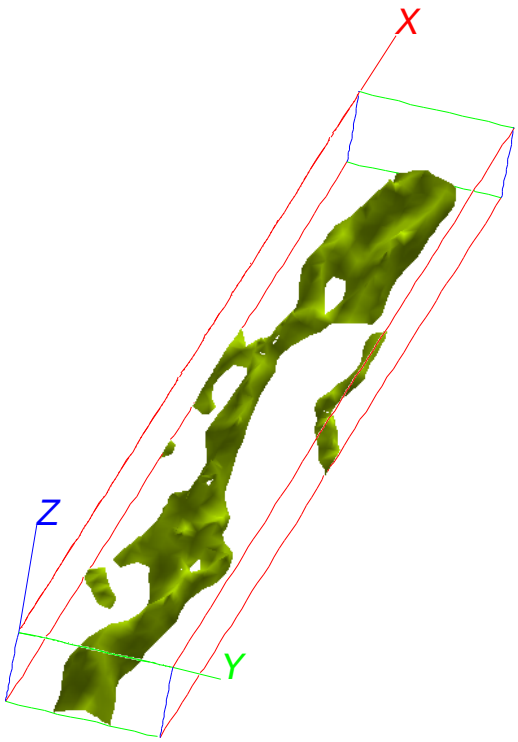

Figure 9. Velocity isosurface describing one isolated low-speed streak. Isosurface velocity value is $0.56\ U_c$. A time-sequence animation of the low-speed streak shown in this Figure may be retrieved at `http://158.110.50.22/turbulent/movie4.htm`

of a minimal channel-flow unit (Jimenez and Moin, 1991), the authors were able to demonstrate that even a vortex-less streak generates new streamwise vortices. With respect to previous pictures of the dynamics of turbulence structures in the wall layer (see Kline et al., 1967, Brooke and Hanratty, 1993, Choi, 2001), somehow the view of evolutionary dynamics of the structures in the boundary layer changes perspective in that streaks are considered responsible for the initial generation of quasi-streamwise vortices. Based on this view, Schoppa and Hussain (1997) conclude by suggesting different strategies for turbulence control. The most interesting strategy seems to be stabilization of the low-speed streaks by means of large-scale forcing motions, given the obvious technological advantages. In practice, a low-speed streak which is more stable to spanwise perturbations would reduce its meandering (see Figure 9) and reduce the tripping frequency of quasi-streamwise vortices (see Figure 10), eventually reducing the frequency and the intensity of turbulence production events −i.e. sweeps and ejections. This suggestion would also explain why turbulent boundary layers loaded with small particles may exhibit reduced drag (Pan and Banerjee, 1996). Small particles characterized by a suitable inertia parameter tend to segregate

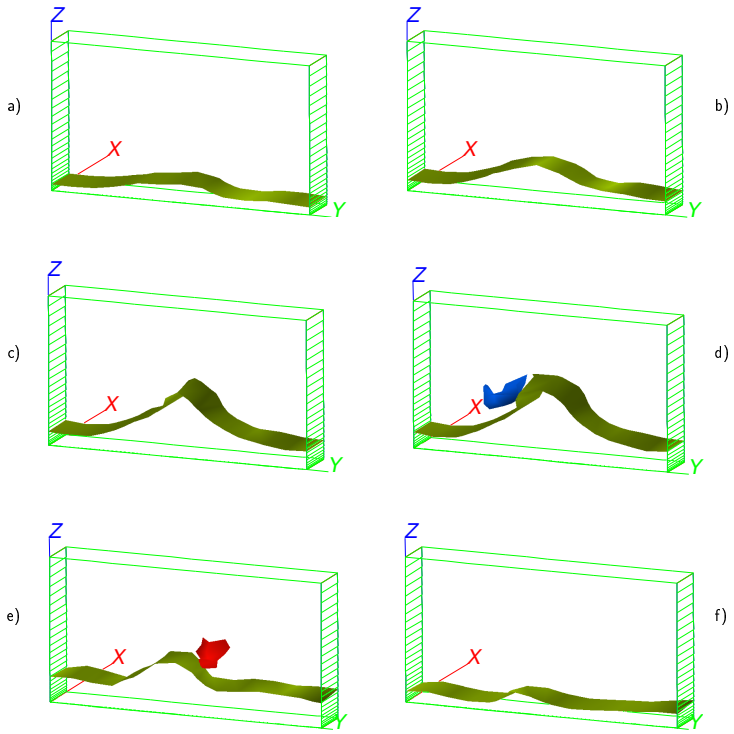

Figure 10. Lagrangian evolution of low-speed streak surface - identified by the $0.56\ U_c$ isosurface - associated with the presence of streamwise vortices - identified by the Ω isosurface: red is clockwise rotating and blue is counterclockwise rotating. The streamwise location is advected downstream with velocity $0.56\ U_c$ (Kim and Hussain, 1993). The wall units time of the different snapshots is a) time 0, b) time 24, c) time 52, d) time 94, e) time 131, and f) time 181. The wall region undergoes modifications from quiescent phase a) and b), to active phase, c) and d) in which the presence of a counterclockwise rotating streamwise vortex is noted, and e) in which the presence of a clockwise rotating streamwise vortex is observed, back to quiescent phase, f). During the time sequence, the initial cross-section advanced about 640 wall units downstream.

into the low-speed streaks. Higher concentrations of particles in the low-speed streaks increase the inertia of the low-speed streaks making them more stable to lateral perturbations.

Large scale forcing of the boundary layer has proven to be effective in a number of previous investigations. For instance, Jung et al. (1992) performed a numerical DNS experiment and were able to reduce drag up to 40% by oscillating the fluid spanwise with respect to the wall —or the wall spanwise with respect to the fluid. Their findings have been later confirmed with other numerical means by Baron and Quadrio (1995). Experimental evidence of drag reduction by spanwise oscillations and explanations of the mechanisms which allow wall oscillations to reduce turbulent drag have been recently provided by Choi and Graham (1998) and by Choi and Clayton (2001). In a number of applications, however, moving the boundary may be unpractical and spanwise motion of the fluid with respect to the wall may be obtained by exploiting body forces.

Recently, Du and Karniadakis (2000) used a direct numerical simulation to verify whether a transverse ElectroMagnetic force could reduce drag in a boundary layer. In their work, arrays of electromagnetic tiles forced a conducting fluid −salt water −and generated a traveling wave only in the viscous sublayer. With this method, they reported drag reduction up to almost 30%.

Starting from this background, we will show different geometries of forcing flows generated by electrostatic forces which can be used to modify turbulence structure at the wall.

3 Forcing Turbulent Boundary Layer with ElectroHydroDynamic Flows

In ESPs, the EHD flows are perceived as detrimental to operation. However, a sound understanding of their interactions with turbulence, could lead to optimization of ESPs in terms of pressure drop and particle collection efficiency. In usual operating conditions, EHD are oriented spanwise with respect to the mean flow (see Figure 1). In the past, the interaction among ESP channel flow and EHD flows generated by both negative and positive discharge have been investigated in various studies which aimed to characterize the fluid dynamic aspects of wire-plate precipitators. Most of this work is experimental (Leonard et al., 1983, Davidson and Shaughnessy, 1986, Davidson and McKinney, 1989, Davidson and McKinney, 1991, Kallio and Stock, 1992), or based on two-dimensional $k-\epsilon$ turbulence models (Bernstein and Crowe, 1981, Kallio and Stock, 1992). The experiments indicate that uniform discharges increase turbulence slightly (Leonard et al., 1983, Kallio and Stock, 1992) or, under certain conditions, decrease turbulence intensity (Leonard et al., 1983), and that tuft discharges (negative discharges) increase turbulence intensity (Leonard et al., 1983, Davidson and Shaughnessy, 1986, Kallio and Stock, 1992). In recent works, we examined this problem using DNS to solve the turbulence field. We found that EHD flows have an effect on drag (Soldati and Banerjee, 1998) and on mass transfer (Soldati, 1998). We also found that this type of EHD flow has a little influence on particle collection efficiency (Soldati, 2000).

In the following section, first we will discuss the characteristics of the complex flow field generated by the interactions among spanwise EHD flows and turbulent channel flow. Second, in the light of the results obtained by Schoppa and Hussain (1998) who were able to obtain large drag reduction by using synthetic −i.e. mathematically generated −streamwise vortical flows, we will present recent results relative to the influence streamwise EHD vortical flows have on turbulence structure at the wall (Fulgosi et al., 1999, Fulgosi et al., 2000).

4 Numerical Simulation

The turbulent flow of air, assumed to be incompressible, Newtonian, with no-slip conditions at walls, and driven by a pressure gradient, was numerically simulated for an imposed pressure gradient in the geometry shown in Figure 1. The wire-electrodes necessary to generate the electrostatic body force to drive the control flows were kept at a potential sufficient to ensure ionic discharge and the presence of distributed ionic species in the duct. Ions are subjected to the Coulomb force, $\mathbf{F}$, which may be expressed as:

$$\mathbf{F} = \rho_c \mathbf{E} \quad , \tag{2}$$

where ρ_c is the charge density and $\mathbf{E}$ is the electric field vector. Ions are driven toward the walls and collide with fluid molecules, transferring momentum to them. This is equivalent to a body force which acts directly on the fluid. Therefore, the equation of fluid motion in dimensional terms is

$$\rho \left[\frac{\partial u_i}{\partial t} + u_j \frac{\partial u_i}{\partial x_j} \right] = -\frac{\partial \mathcal{P}}{\partial x_i} + \mu \frac{\partial^2 u_i}{\partial x_j \partial x_j} + F_i \quad , \tag{3}$$

where u_i are the dimensional velocity components along the three directions x_i (with x_1, or x being streamwise, x_2 or y being spanwise and x_3 or z being the wall-normal directions), $\mathcal{P}$ is pressure, and ρ and μ are fluid density and dynamic viscosity, respectively. For the cases under consideration, the body force distribution does not fluctuate because of ionic convection. This is a realistic assumption, since ions have a drift velocity of about a hundred meters per second in air while the mean flow velocity is about one meter per second. For liquids, ionic convection may not be negligible and "two-way" coupling will exist between the flow field and the electrostatic body force field. Here the coupling is "one-way", i.e. the flow field does not modify the electrostatic body forces.

4.1 Flow Field

The flow field was calculated by integrating mass and momentum balance equations in dimensionless form obtained using the duct half-width, h, and the shear velocity, u_τ, defined as

$$u_\tau = \sqrt{\frac{\tau_w}{\rho}} \tag{4}$$

where τ_w is the shear at the wall. Therefore, mass and momentum balance equations in dimensionless form are

$$\frac{\partial u_i}{\partial x_i} = 0 \quad , \tag{5}$$

and

$$\frac{\partial u_i}{\partial t} = -u_j \frac{\partial u_i}{\partial x_j} + \frac{1}{Re} \frac{\partial^2 u_i}{\partial x_j \partial x_j} - \frac{\partial p}{\partial x_i} + \delta_{1,i} + \Phi_i \quad , \tag{6}$$

where u_i is the ith component of the dimensionless velocity vector, $\delta_{1,i}$ is the mean dimensionless pressure gradient, Φ is the dimensionless electrostatic body force, and $Re_\tau = h u_\tau / \nu$ is the shear Reynolds number. Eqs. 5 and 6 were solved directly using a pseudo-spectral method similar to that used by Kim et al. (1987) to solve the turbulent, closed-channel-flow problem. The difference is the inclusion of the space-dependent body force which, being steady and uncoupled to the flow field, was calculated once at the beginning of each simulation. If the body force term is treated together with the nonlinear terms, Eq. 6 may be recast as:

$$\frac{\partial u_i}{\partial t} = S_i + \frac{1}{Re_\tau} \frac{\partial^2 u_i}{\partial x_j \partial x_j} - \frac{\partial p}{\partial x_i} \tag{7}$$

which is identical to forms previously solved (Kim et al., 1987, Lam and Banerjee, 1992), and where S_i now includes the convective term, the mean pressure gradient and the Coulomb term. The pseudo-spectral method is based on transforming the field variables into wave-number space, using Fourier representations for the streamwise and spanwise directions and a Chebyshev representation for the wall-normal (nonhomogeneous) direction. A two-level, explicit, Adams-Bashforth scheme for the nonlinear terms S_i and an implicit Crank-Nicolson method for the viscous terms were employed for time advancement. Details of the method have been published previously (Lam and Banerjee, 1992).

Considering air with density of $1.38\ kg/m^3$, and kinematic viscosity of $16.6 \cdot 10^{-6}\ m^2/s$, since the pressure gradient is equal for all simulations, the shear velocity is $8.964 \cdot 10^{-2}\ m/s$, and the shear Reynolds number is equal to 108. For the reference case with no EHD effects, the mean velocity is $1.16\ m/s$ and the Reynolds number based on mean velocity and duct width is ~ 2795.

4.2 Body Force Control Field

The electrostatic potential distribution and space charge distribution are given by the following set of equations:

$$\frac{\partial^2 V}{\partial x_i^2} = -\frac{\rho_c}{\epsilon_0} \tag{8}$$

$$\rho_c^2 = \epsilon_0 \frac{\partial \rho_c}{\partial x_i}\frac{\partial V}{\partial x_i} = -\epsilon_0 \frac{\partial \rho_c}{\partial x_i} E_i \tag{9}$$

$$E_i = -\frac{\partial V}{\partial x_i} \tag{10}$$

$$J_i = -\rho_c \beta E_i \quad . \tag{11}$$

where, ϵ_0 is air permittivity ($\epsilon_0 = 8.854 \cdot 10^{-12}$), and $\beta = 1.4311 \cdot 10^{-4} m^2/V\ s$ is ionic mobility (Mc Daniel and Mason, 1973) for positive discharge in air. Eqs. 8-11 were solved by a two dimensional finite difference scheme (Leutert and Bohlen, 1972) based on an initial guess for the space charge density at the wire followed by iterative solution of Eqs. 8 and 9 until convergence of the plate current density was obtained. Details on the numerical procedure and on the validation of the body force calculation against previous numerical and experimental analysis may be found in previous works (Kallio and Stock, 1986).

The problem investigated is described by the balance equation for the fluid and a reduced set of Maxwell equations for the electrostatic body force distribution (Soldati and Banerjee, 1998), which, being decoupled from the flow field, can be calculated once for all and regardless of how the flow field evolves. We use a two-dimensional finite-difference method to calculate the electrostatic body force field (Soldati and Banerjee, 1998, Fulgosi, 1998).

5 Forcing Turbulence with Spanwise EHD Flows

The effect of spanwise EHD flows on turbulence structure was investigated for one low, and one high, intensity level of the electrostatic body force. A previous channel simulation, without EHD effects, at the same shear Reynolds number (Soldati et al., 1993) was used as a reference for comparison purposes. The flow field was examined by a triple decomposition, discussed later. Various parameters were chosen so as to obtain electrohydrodynamic conditions similar to those used in practice, and in previous investigations. A nondimensional number enters the problem, representing the ratio between the electrostatic body force and inertial forces acting on a fluid parcel (Yamamoto and Velkoff, 1981, Leonard et al., 1983, Davidson and Shaughnessy, 1986). This is called ElectroHydrodynamic Number, N_{EHD}. In Leonard et al. (1983), and in this paper,

$$N_{EHD} = \frac{i}{l\,\rho\,\beta\,U^2} \ , \tag{12}$$

where i represents the total current at the plate, l the length of the wire, and U the mean flow velocity. In the limiting case of $N_{EHD} = 0$, the flow is unaffected by electrohydrodynamic forces (i.e. it is channel flow). In the limiting case $N_{EHD} = \infty$, the through flow does not affect EHD flows. In the present investigation, two different simulations were run with $N_{EHD1} = 1.1$ and $N_{EHD2} = 2.5$. These are in the range used in previous work, i.e. Kallio and Stock (1992), used N_{EHD} from 0.6 to ~ 8, Leonard et al. (1983) used N_{EHD} from 0 to 2.4. This range is representative of actual electrostatic precipitators. For the low intensity case, the linear current density at the plate was $I_1 = 0.3 \cdot 10^{-3} A/m$, with a potential at the wire of $V_1 = 32\ 000$. In the high intensity case, the linear current density at the plate was $I_1 = 0.75 \cdot 10^{-3} A/m$, with a potential at the wire of $V_1 = 42\ 000$. Again, these values are typical of industrial electrostatic precipitators. From the fluid motion viewpoint, the wires are not taken into consideration, as they are usually rather fine and wake effects are shown to be small in comparison with EHD effects. Simulations presented here were run with $128 \times 64 \times 65$ nodes in a box of dimensionless size $1357 \times 678 \times 216$ in wall units (dimensionless variables in wall units are indicated by the superscript $+$) and a time step $\Delta t^+ = 0.038$. This gives a resolution of $\Delta x_1^+ = 10.6$, $\Delta x_2^+ = 10.6$, and Δx_3^+ ranging from 0.13 next to the walls to 5.3 in the center of the channel. For both cases, the simulations were started from the steady turbulent channel flow computed in Soldati et al. (1993) by turning on the electrostatic body force.

When the flow field become statistically steady, the results were stored for a sufficient number of time steps to allow reliable calculations of the turbulence statistics and the energy budget.

5.1 Mean Quantities: drag reduction due to EHD flows

EHD flows generate no mean flow directly. Since they modify the turbulence field, influencing turbulent transfer mechanisms, mean flow variables may be expected to vary. To obtain correct values for the mean variables, averages must be obtained both in time and in the homogeneous directions (i.e. averaged over the $x - y$ plane). In Figure 11, the mean velocity profile calculated for the low and high N_{EHD} cases is compared with that of turbulent channel flow (Soldati et al., 1993). Since the wall shear stress is held constant in the simulations, an increase in mean velocity indicates drag reduction whereas a decrease in mean velocity indicates drag increase. The mean velocity in channel flow is about $1.16\ m/s$: it increases to $1.19\ m/s$ ($\sim 3\%$) in the low N_{EHD}

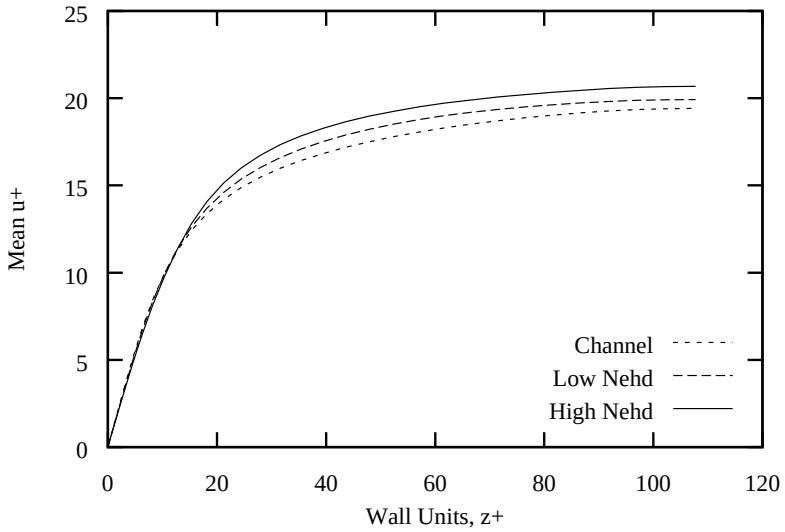

Figure 11. Mean velocity of flow in the duct for channel flow, for low N_{EHD} and for high N_{EHD}.

case and up to $1.23\ m/s$ ($\sim 6\%$) in the high N_{EHD} case. Thus, the value of the N_{EHD} number is 1.1 in the low intensity case and 2.5 in the high intensity case, and the Reynolds number based on mean velocity and duct width is ~ 2857 in the low N_{EHD} case and 2964 in the high N_{EHD} case. As drag varies approximately as the square of the mean velocity, the low N_{EHD} case results in $\sim 6\%$ drag reduction, whereas in the high N_{EHD} case the reduction is $\sim 12\%$.

Since EHD forces do not generate mean through-flow directly, in previous work (Davidson and Shaughnessy, 1986, Kallio and Stock, 1992), attention was not paid to differences in the mean through-flow for a given pressure gradient.

5.2 Triple Decomposition: Filtering of the Flow Field

EHD vortices are organized coherent structures. In order to separate the effect of these organized spanwise vortices from the turbulent flow field, and to clarify the role of EHD flows on turbulence modification, field variables, $f(x,y,z,t)$, were decomposed as:

$$f(x,y,z,t) = \overline{f}(z) + \tilde{f}(x,z,t) + f'(x,y,z,t) \quad , \tag{13}$$

where

$$\tilde{f} = < f > - \overline{f} \quad ,$$

and $\overline{f}$ is the space average over the homogeneous directions (x and y), $< f >$ is the phase average (the average over the spanwise direction in the present case), representing the organized EHD field, and f' is the instantaneous turbulent fluctuation. Similar decompositions have been applied previously to investigate the influence of an organized wave on a turbulent channel flow (Reynolds and Hussain, 1972, Harris and Street, 1994) and in discussions related to coherent structures in turbulent flows (Hussain, 1983).

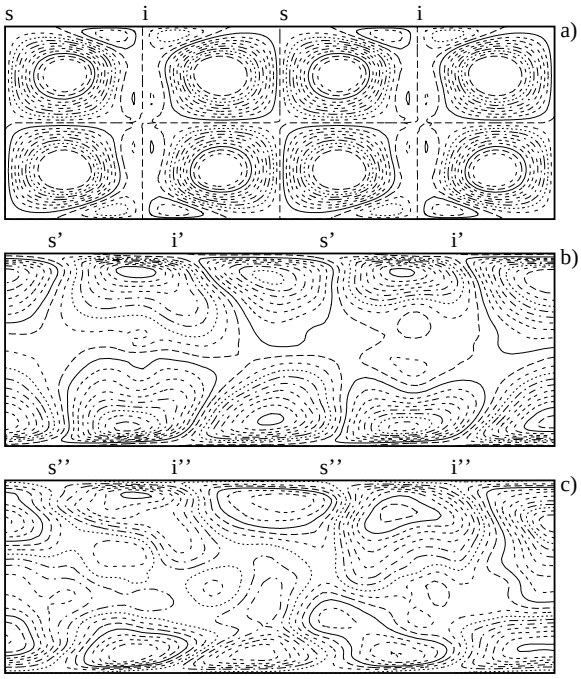

Figure 12. Isocontours of streamlines of EHD flows in three cases: a) $N_{EHD} = \infty$, with contours going from -1 to 1 with 0.1 increments in wall units; b) $N_{EHD} = 2.5$ with contours going from -0.27 to 0.3 with 0.03 increments in wall units; c) $N_{EHD} = 1.1$, with contours going from -0.12 to 0.18 with 0.015 increments in wall units; Distortion of upstream and downstream vortices is uneven. Upstream flows have larger gradients but smaller extent than downstream flows.

5.3 Filtered EHD Flows

A detailed picture of the recirculating structure of EHD flows is evident from the streamline plots in Figure 12, where a portion of the domain again containing two wires is shown. Consider the no-flow case: each wire generates four equal vortical cells, two upstream and two downstream from the wire. For decreasing N_{EHD}, the vortical cells lose coherence, and intensity, and fluctuate in shape. In previous work (Lai et al., 1995), oscillations of the vortical cells have been found in simulations of two-dimensional viscous flows, for N_{EHD} above a critical value of ~ 5. In the present work, the oscillations of the vortical cells are likely to be due also to the fluctuating character of the interactions with the turbulence field, which induce a slight dependence on time of the EHD flows. The instantaneous plots of Figures 12 b) and c), may be used to examine the modifications to the vortical cells caused by the turbulent through-flow. As N_{EHD} decreases, the initially symmetric cells upstream and downstream of the wires become different. Upstream cells tend to assume a trapezoidal shape, while downstream cells take on a triangular shape, similar to previous findings in the viscous regime (Yamamoto and Velkoff, 1981, Lai et al.,

1995). The upstream flows encounter an adverse pressure gradient, while downstream flows find a favorable one. Therefore, the upstream branch of the upstream vortex tends to stay attached to the wall, displacing the downstream branch of the neighboring vortex from the wall. In contrast, the downstream branch of the upstream vortex is advected downstream, reducing the extent of the upstream branch of the downstream vortex, also counteracted by the stronger mean flow velocity field in the center of the channel.

Vortical cells appear also to be *squeezed* towards the wall for decreasing N_{EHD}. If N_{EHD} is reduced, the region where EHD flows can compete with the mean flow, and so maintain their identity, becomes increasingly smaller, and more confined to the wall region.

In Figure 12 a), stagnation points are located at equally spaced intervals. The through-flow displaces the stagnation points downstream and changes the spacing between them. Two different types of stagnation points may be identified. The first (an "i" point) generated by impingement of the jet on the wall, and the second (an "s" point) generated by the return flow toward the center of the channel. Stagnation points appear to be steady, i.e. no appreciable displacements due to turbulent fluctuations were observed. The downstream displacements of "i" points are $0.40\ h$ in both high and low N_{EHD} cases, whereas downstream displacements of "s" points are $0.62\ h$ in the high N_{EHD} case and $0.64\ h$ in the low N_{EHD} case. In the no-flow case, the vortical cells are $1.57\ h$ wide.

When the turbulent through-flow is imposed, the upstream vortex is $\sim 1.34\ h$ in streamwise extent, whereas the downstream vortex is about a third larger, being about $1.80\ h$ in extent. For the N_{EHD} numbers investigated, there are no significant differences in the dimensions of the vortical cells in the low and high N_{EHD} cases. It is clear that the through-flow reduces the intensity of EHD flows. In our simulations, the maximum wall-normal velocity (found in the wire-section of the no-flow case and slightly downstream in the through-flow cases) decreases from about $0.95\ m/s$ down to $0.11\ m/s$ for the conditions of the high N_{EHD} case, and from about $0.45\ m/s$ to approximately $0.04\ m/s$ for the conditions of the low N_{EHD} case $-$ a reduction of about an order of magnitude. The maximum value of the streamwise velocity is reduced by less, falling from $0.8\ m/s$ to $0.34\ m/s$, for the high N_{EHD} case, and from $0.38\ m/s$ to $0.15\ m/s$ for the low N_{EHD} case. The maximum values of the streamwise component are found in the upstream branch of the upstream vortical cell.

In order to validate these findings, qualitative comparisons were made with experimental data. The Reynolds numbers of the simulations were necessarily lower owing to computer resources. For instance, experimental data of Kallio and Stock (1992), who measured the velocity of the EHD jets toward the walls were obtained in a three-wire precipitator $20.32\ cm$ wide, with a wire-to-wire spacing of $20.32\ cm$. For an applied voltage of $42\ 000\ V$, the linear current density was $I = 0.5 \cdot 10^{-3} A/m$, which, in their experiments with mean flow velocity of $1\ m/s$, gives $N_{EHD} \simeq 2.5$. Kallio and Stock (1992) presented results for the time-averaged wall-normal velocity of the particle-seeds in the section corresponding to a wire, and in that corresponding to the midpoint between two wires. Since they also provided an estimate of the Coulomb drift of particle-seeds, it is possible to compare their findings against our simulation for the high N_{EHD} case. However, the Reynolds number based on mean flow velocity and duct width was more than $12\ 000$ for their experiments $-$ about four times larger than ours $-$ and since their precipitator was larger than ours, their EHD structures were stronger than those obtained in the present work. For these reasons, the results of our solution can be compared against their experimental data only on a qualitative basis.

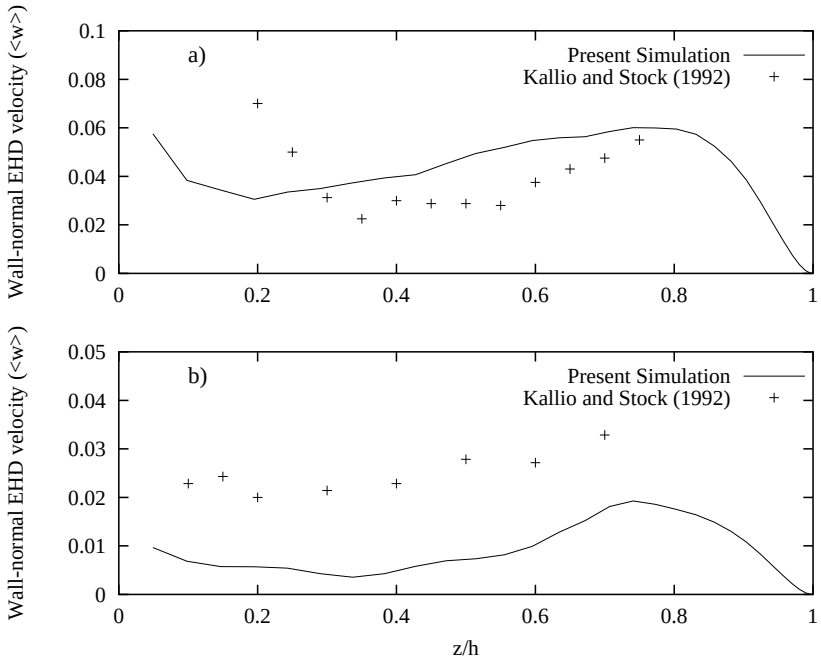

Figure 13. Comparison of profiles of organized wall-normal component of EHD flows from the present simulations against data by Kallio and Stock (Kallio and Stock, 1992): a) cross-section corresponding to wire; b) cross-section corresponding to midpoint between two wires. Velocity is measured in m/s.

In Figure 13, where velocity has dimensions of meters per second, data are compared against the time-average of the EHD organized component in the high N_{EHD} case. Figure 13 a) refers to the streamwise section, corresponding to the wire and Figure 13 b) corresponds to the midpoint between two wires. Though there are significant differences between experimental data and the present simulation, the qualitative behavior of the velocity field in the EHD structures is similar.

5.4 Statistics of the Turbulence Field

The filtered statistics of the turbulent velocity field give information on the distribution and intensity of turbulent fluctuations. The effects of EHD flows on turbulence intensity may be appreciated in Figure 14, where the RMS values of the velocity fluctuations in all three directions are shown. Turbulence intensity decreases in all directions in the low N_{EHD} case. With increasing N_{EHD}, turbulence intensity increases in the streamwise direction and in the wall-normal direction. It is clear that EHD flows exert a damping action on turbulence at low N_{EHD}, but they also promote turbulence generation, an effect which becomes important at higher N_{EHD}. As we will see later, this does not mean, however, that the Reynolds stress, $-\overline{u'w'}$, increases for the high N_{EHD} case.

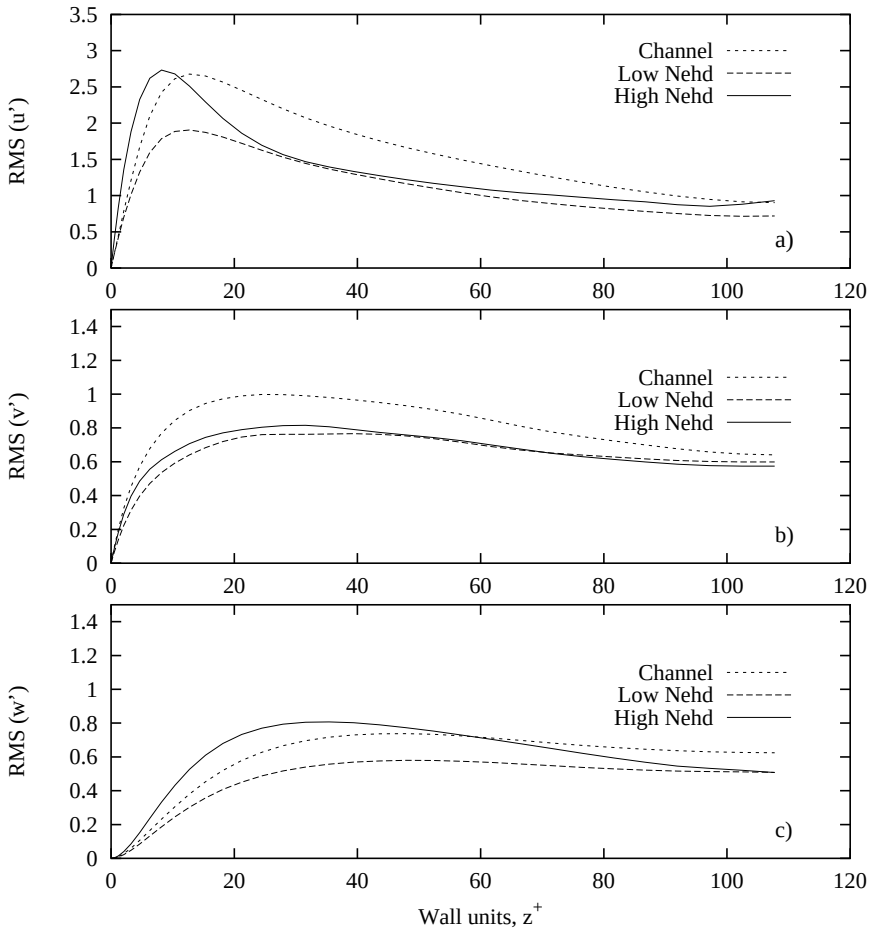

Figure 14. Root mean square of turbulent velocity fluctuations for channel flow, low N_{EHD}, and high N_{EHD}: a) streamwise component; b) spanwise component; c) wall-normal component. In the low N_{EHD} case, turbulence intensity is reduced in all directions. In the high N_{EHD} case, turbulence production by EHD flows is evident in the streamwise direction – in the wall region – and in the wall-normal direction.

5.5 Quadrant Analysis

The drag reduction caused by EHD flows as observed through the increase of the mean flow (Figure 11) is confirmed by the behavior of the $-\overline{u'w'}$ Reynolds stress, shown in Figure 15. In the low N_{EHD} case, the variations of the Reynolds stress are small, and mostly relative to the peak; in the high N_{EHD} case, the profile differs substantially from that of channel flow, particularly in the wall region. In the region far from the wall, all three profiles appear to collapse onto each other.

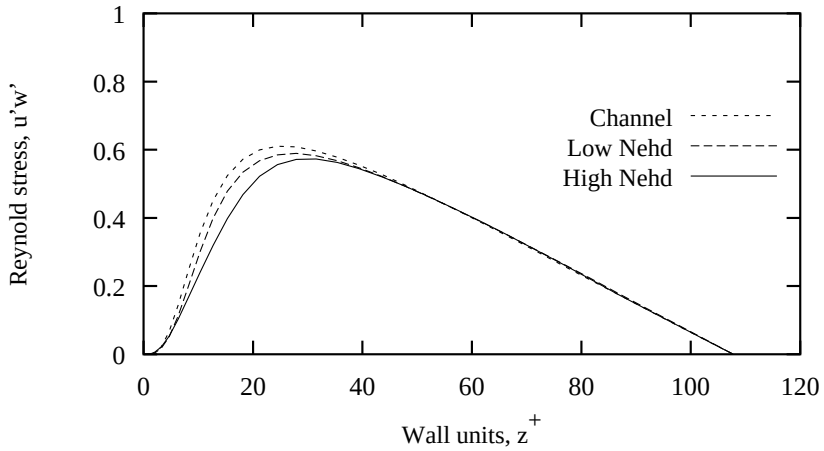

Figure 15. Profile of Reynolds stress $-\overline{u'w'}$ filtered from organized component for channel flow, low N_{EHD}, and high N_{EHD}.

In Figure 16, the fractional contribution of each type of event to the $-\overline{u'w'}$ Reynolds stress is presented for the low and high N_{EHD} cases compared to channel flow. The presence of EHD flows modifies the balance among the different quadrants, which exists in channel flow (see Figure 3). This is evident mostly in the wall region. At low EHD flow intensity, sweep events are practically unaffected by EHD flows, whereas first, second and third quadrant event contributions are all increased. At high EHD flow intensity, variations are large in all quadrants. The overall effect of EHD flows in the wall region is thus to increase the intensity of the events from all quadrants, both by increasing the intensity of the fluctuations and the correlation between streamwise and wall-normal fluctuations. However, the increase of the positive Reynolds stress contributions, i.e. first and third quadrants, is larger compared to that of the negative Reynolds stress contributions, i.e. second and fourth quadrants, thus leading to an overall reduction of the drag. Analyzing the frequency of the events (Soldati and Banerjee, 1997), we found that, in the wall region, EHD flows decrease all the events that give negative Reynolds stress from the second and fourth quadrants and increase those that give positive Reynolds stress from first and third quadrants – explaining drag reduction.

5.6 Influence of Spanwise EHD Flows on Mass Transfer at the Wall

Since turbulence transfer rates are controlled by quadrant events, we examined also the influence of EHD flows on mass transfer at the wall. In ESPs applications, this can be relevant for emission control (Dinelli and Rea, 1990, Dinelli et al., 1991).

In previous works (Campbell and Hanratty, 1983, Pan and Banerjee, 1996), the averaged turbulent mass transfer at a solid wall was expressed as:

$$\overline{K} \sim S^{-0.7}\overline{(\kappa^2)}^{0.21} \quad , \tag{14}$$

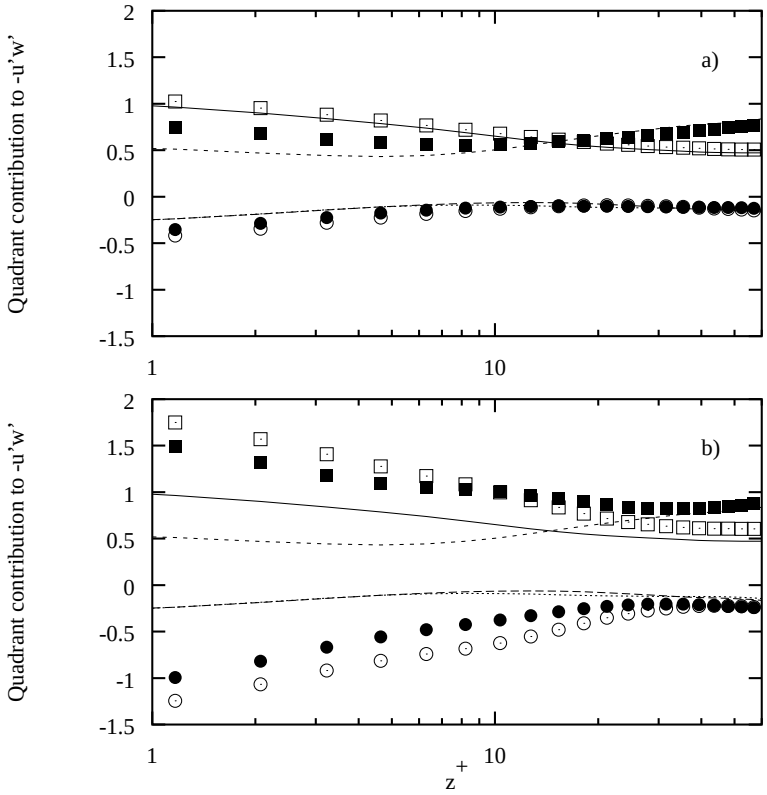

Figure 16. Comparison of quadrant analysis for channel flow, a) low N_{EHD}, and b) high N_{EHD}. Lines and symbols represent the values for channel flow and channel flow with EHD effects respectively: (•) and (– – –) first quadrant events; (■) and (-----) second quadrant events; (∘) and (· · · · ·) third quadrant events; (□) and (——) fourth quadrant events.

in which S is the Schmidt number, and κ is a function related to the behavior of the normal velocity fluctuations, w', and can be expressed as:

$$w'(x,y,z,t) = \kappa(x,y,z,t)z^2 \ . \tag{15}$$

Since the behavior of the normal fluctuations is changed by the EHD flows (Soldati and Banerjee, 1997), the mass transfer coefficient is changed as well. In Figure 17, the behavior of the function $\overline{\kappa^2}$ is presented for the cases of channel flow, low and high N_{EHD} respectively. It can be observed that low intensity EHD flows decrease the wall-normal velocity fluctuations, whereas high intensity EHD flows increase them. This suggests that EHD flows organized structures might be used also to modify and control mass transfer characteristics of a turbulent flow.

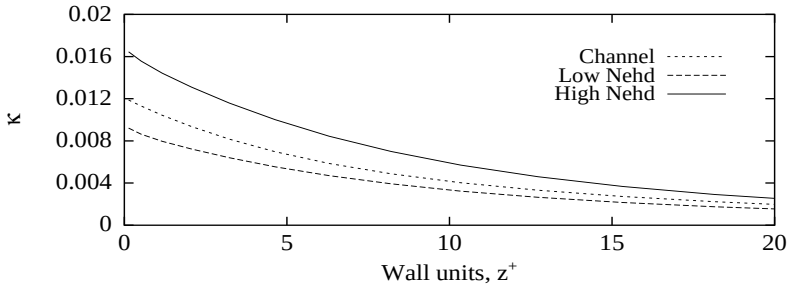

Figure 17. EHD flows effect on the wall mass transfer coefficient, κ, in turn connected to the behavior on the near-wall normal velocity fluctuations.

5.7 The Governing Equations and Energy Balance Considerations

Insight into the dynamics of the flow field, and in particular into the mechanisms of turbulence production by EHD flows, may be gained by examining the equations of motion for each component. The continuity equation for the three fields are obtained by applying triple decomposition (Equation 13) to the continuity equation (Equation 5), and then phase-averaging, and space-averaging, over the homogeneous components. The continuity equations for all components of the flow field are

$$\frac{\partial \overline{u}_i}{\partial x_i} = \frac{\partial \tilde{u}_i}{\partial x_i} = \frac{\partial u_i'}{\partial x_i} = 0 \quad . \tag{16}$$

A similar procedure is adopted for the momentum balance equations, i.e. by substituting Eq. 13 into Eq. 6, and phase averaging, we obtain the following equation,

$$\frac{\partial \tilde{u}_i}{\partial t} + \overline{u}_j \frac{\partial \overline{u}_i}{\partial x_j} + \overline{u}_j \frac{\partial \tilde{u}_i}{\partial x_j} + \tilde{u}_j \frac{\partial \overline{u}_i}{\partial x_j} + \frac{\partial}{\partial x_j} < u_i' u_j' > + \frac{\partial}{\partial x_j}(\tilde{u}_i \tilde{u}_j) =$$

$$= \frac{1}{Re}\left(\frac{\partial^2 \overline{u}_i}{\partial x_j \partial x_j} + \frac{\partial^2 \tilde{u}_i}{\partial x_j \partial x_j} \right) - \frac{\partial \overline{p}}{\partial x_i} - \frac{\partial \tilde{p}}{\partial x_i} + \tilde{\Phi}_i \quad . \tag{17}$$

which, averaged over the homogeneous components, gives the equation for the mean field:

$$\overline{u}_j \frac{\partial \overline{u}_i}{\partial x_j} = -\frac{\partial \overline{p}}{\partial x_i} + \frac{1}{Re} \frac{\partial^2 \overline{u}_i}{\partial x_j \partial x_j} - \frac{\partial}{\partial x_j}(\overline{u_i' u_j'}) - \frac{\partial}{\partial x_j}(\overline{\tilde{u}_i \tilde{u}_j}) \quad . \tag{18}$$

As expected, there is no direct generation of mean flow by the body forces. The equation of motion for the organized EHD flows is obtained by subtracting Eq.18 from Eq.17. Therefore,

$$\frac{\partial \tilde{u}_i}{\partial t} + \overline{u}_j \frac{\partial \tilde{u}_i}{\partial x_j} + \tilde{u}_j \frac{\partial \overline{u}_i}{\partial x_j} =$$

$$= -\frac{\partial \tilde{p}}{\partial x_i} + \frac{1}{Re} \frac{\partial^2 \tilde{u}_i}{\partial x_j \partial x_j} + \frac{\partial}{\partial x_j}\left(\overline{\tilde{u}_i \tilde{u}_j} - \tilde{u}_i \tilde{u}_j \right) + \frac{\partial}{\partial x_j}\left(\overline{u_i' u_j'} - < u_i' u_j' > \right) + \tilde{\Phi}_i \quad . \tag{19}$$

In this equation, the term $\tilde{\Phi}$ is the electrostatic body force which drives the EHD flows (it is clear that $\tilde{\Phi} = \Phi$). The equation for the turbulent component of the flow field is obtained by subtracting Eq. 17 from Eq. 6. This gives

$$\frac{\partial u_i'}{\partial t} + \overline{u}_j \frac{\partial u_i'}{\partial x_j} + u_j' \frac{\partial \overline{u}_i}{\partial x_j} + \tilde{u}_j \frac{\partial u_i'}{\partial x_j} + u_j' \frac{\partial \tilde{u}_i}{\partial x_j} = -\frac{\partial p'}{\partial x_i} + \frac{1}{Re} \frac{\partial^2 u_i'}{\partial x_j \partial x_j} +$$

$$+ \frac{\partial}{\partial x_j} \left(< u_i' u_j' > - u_i' u_j' \right) \ . \tag{20}$$

The term $-\overline{\tilde{u}_i \tilde{u}_j}$ is the organized Reynolds stress (or the EHD supported stress), appearing both in the equation for the mean field and for the organized motion. It represents the contribution of the organized flows to the transport of mean momentum. Analogously, the term $-\overline{u'_i u'_j}$ represents the contribution of the turbulence field to the mean momentum transport. Following Hussain (1983), the momentum transport due to the turbulent field, $r'_{ij} = -u'_i u'_j$, may be viewed as:

$$r'_{ij} = \overline{r}_{ij} + \tilde{r}_{ij} + r_{ij} \ ,$$

where,

$$\begin{aligned} \overline{r}_{ij} &= -\overline{u_i' u_j'} \ , \\ \tilde{r}_{ij} &= - < u_i' u_j' > + \overline{u_i' u_j'} \ , \\ r_{ij} &= -u_i' u_j' + < u_i' u_j' > \ . \end{aligned}$$

These terms represent the contribution of the turbulent field to the momentum transport of the three fields: $\overline{r}_{ij}$ is the turbulent contribution to the mean momentum transport; $\tilde{r}_{ij}$ is the turbulent contribution to the organized momentum transport; and r_{ij} is the turbulent contribution to the turbulent momentum transport. In particular, $\tilde{r}_{ij}$ is the difference between the phase and space averages of the turbulent Reynolds stress, and can be interpreted as the oscillation of the turbulent Reynolds stress due to the presence of the periodic pattern.

We will now examine the energy fluxes which couple the three fields through analysis of the kinetic energy transport equations.

On application of Eq. 13, the total kinetic energy, $1/2\overline{u_i u_i}$ may be expressed as the sum of the kinetic energy associated with the mean field, that associated with the organized motions and that associated with the turbulence field as

$$\frac{1}{2}\overline{u_i u_i} = \frac{1}{2}\overline{u}_i \overline{u}_i + \frac{1}{2}\overline{\tilde{u}_i \tilde{u}_i} + \frac{1}{2}\overline{u_i' u_i'} \ .$$

By multiplying the momentum equation for $\overline{u}_i$ (Eq. 18), by $\overline{u}_i$, phase-averaging and averaging over the homogeneous directions, we obtain the mean field kinetic energy transport equation:

$$\frac{\overline{D}}{Dt}\left(\frac{1}{2}\overline{u}_i \overline{u}_i\right) = -\frac{\partial}{\partial x_j}\left(\overline{p}\overline{u}_j\right) - \underbrace{\left(-\overline{u_i' u_j'}\right)\frac{\partial \overline{u}_i}{\partial x_j}}_{\text{I}} - \underbrace{\left(-\overline{\tilde{u}_i \tilde{u}_j}\right)\frac{\partial \overline{u}_i}{\partial x_j}}_{\text{II}} - \frac{\partial}{\partial x_j}\left[\overline{u}_i \left(\overline{u_i' u_j'} + \overline{\tilde{u}_i \tilde{u}_j}\right)\right]$$

$$+\frac{1}{Re}\frac{\partial^2}{\partial x_j^2}\left(\frac{1}{2}\overline{u}_i\overline{u}_i\right) - \frac{1}{Re}\frac{\partial \overline{u}_i}{\partial x_j}\frac{\partial \overline{u}_i}{\partial x_j} \quad . \tag{21}$$

Analogously, by multiplying the momentum equation for $\tilde{u}_i$ (Eq. 19) by $\tilde{u}_i$, phase-averaging and averaging over the homogeneous directions, we obtain the organized field kinetic energy transport equation:

$$\frac{\overline{D}}{Dt}\left(\frac{1}{2}\overline{\tilde{u}_i\tilde{u}_i}\right) = -\frac{\partial}{\partial x_j}\left[\overline{\tilde{u}_j\left(\tilde{p}+\frac{1}{2}\tilde{u}_i\tilde{u}_i\right)}\right] + \underbrace{\left(-\overline{\tilde{u}_i\tilde{u}_j}\right)\frac{\partial \overline{u}_i}{\partial x_j}}_{\text{II}} \quad \underbrace{-\overline{\left(-<u_i'u_j'>\right)\frac{\partial \tilde{u}_i}{\partial x_j}}}_{\text{III}} +$$

$$-\frac{\partial}{\partial x_j}\left(\overline{\tilde{u}_i<u_i'u_j'>}\right) + \frac{1}{Re}\frac{\partial^2}{\partial x_j^2}\left(\frac{1}{2}\overline{\tilde{u}_i\tilde{u}_i}\right) - \frac{1}{Re}\overline{\frac{\partial \tilde{u}_i}{\partial x_j}\frac{\partial \tilde{u}_i}{\partial x_j}} + \overline{\tilde{u}_i\tilde{\Phi}_i} \quad . \tag{22}$$

Finally, by multiplying the momentum equation for u_i' (Eq. 20) by u_i', phase-averaging and averaging over the homogeneous directions, the turbulence field kinetic energy transport equation is obtained:

$$\frac{\overline{D}}{Dt}\left(\frac{1}{2}\overline{u_i'u_i'}\right) = -\frac{\partial}{\partial x_j}\left[\overline{u_j'\left(p'+\frac{1}{2}u_i'u_i'\right)}\right] + \underbrace{\left(-\overline{u_i'u_j'}\right)\frac{\partial \overline{u}_i}{\partial x_j}}_{\text{I}} \quad + \underbrace{\overline{\left(-<u_i'u_j'>\right)\frac{\partial \tilde{u}_i}{\partial x_j}}}_{\text{III}} +$$

$$-\overline{\tilde{u}_j\frac{\partial}{\partial x_j}<\frac{1}{2}u_i'u_i'>} + \frac{1}{Re}\frac{\partial^2}{\partial x_j^2}\left(\frac{1}{2}\overline{u_i'u_i'}\right) - \frac{1}{Re}\overline{\frac{\partial u_i'}{\partial x_j}\frac{\partial u_i'}{\partial x_j}} \quad . \tag{23}$$

In Eqs. 21, 22 and 23, the l.h.s. is the material rate of change of the mean, organized and turbulent kinetic energy, respectively. This term is zero in steady flows. The energy from the electrostatic body force field which produces the EHD flows is the last term of Eq. 22, $\overline{\tilde{u}_i\tilde{\Phi}_i}$. The terms identified as I, II and III are the energy fluxes that couple the three fields. Term I is the production of turbulence by the action of the turbulent Reynolds stresses against the mean strain rate. This term appears as a drain term in Eq. 21 and as a source term in Eq. 23. Analogously, term II is the production of disturbance energy by action of the mean field, through the mean strain rate, against the organized flow Reynolds stresses.

This term drains energy from the mean field toward the organized field. The energy coupling between the turbulent field and the organized field is given by term III, which is the turbulent kinetic energy produced by the organized EHD flows through the phase-averaged turbulent Reynolds stresses. Term III appears as a source of turbulent kinetic energy in Eq. 23.

5.8 Turbulence Kinetic Energy Budget

As pointed out by Hunt (1995), the direct effect of the body force field on the kinetic energy of turbulence is zero. However this force has a significant indirect effect on the turbulence kinetic energy budget.

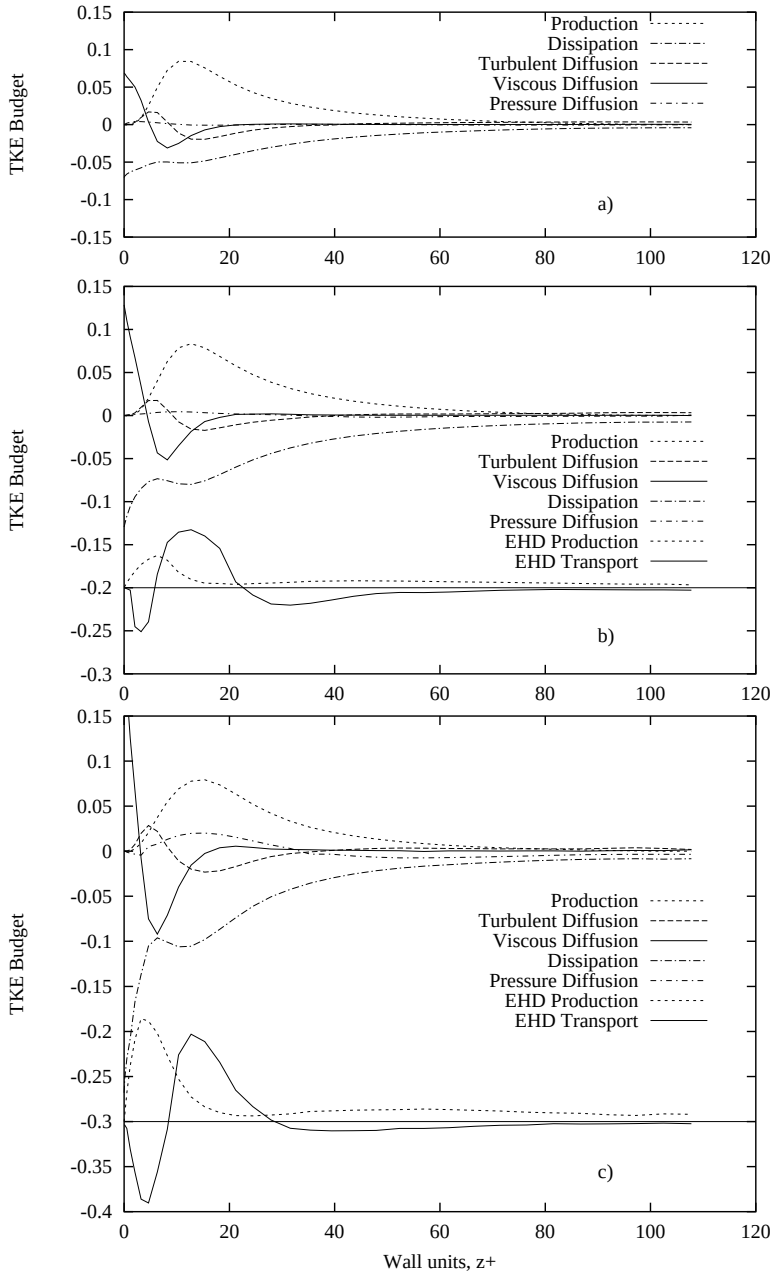

Figure 18. Turbulent kinetic energy budget: a) channel flow; b) low N_{EHD}; c) high N_{EHD}. New terms of energy input and transfer are generated by EHD flows: turbulence production by EHD flows and turbulence transfer by EHD organized motions. For clarity of presentation, the zero of these new terms is shifted by -0.2 in the low N_{EHD} case and by -0.3 in the high N_{EHD} case. All terms made dimensionless by u_τ^4/ν.

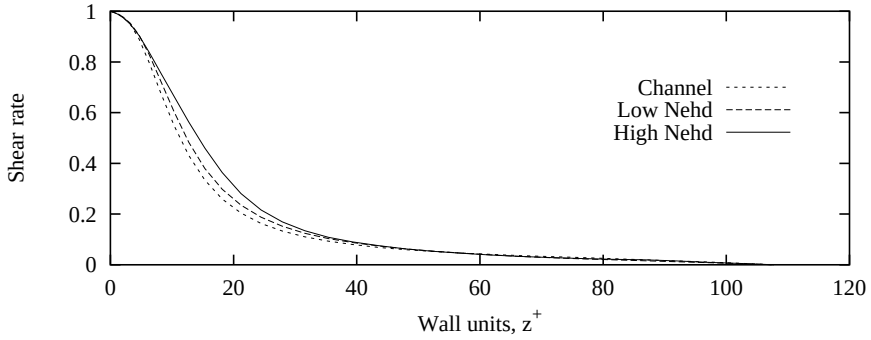

Figure 19. Profile of shear rate in the duct for channel flow, low N_{EHD}, and high N_{EHD}.

To analyze in detail the effect of EHD flows on transfer and production of turbulence kinetic energy, we will rewrite Eq. 23 in the following form:

$$0 = -\overline{u_i' u_j'}\frac{\partial \overline{u}_i}{\partial x_j} - \frac{1}{Re}\overline{\frac{\partial u_i'}{\partial x_j}\frac{\partial u_i'}{\partial x_j}} + \overline{p'\frac{\partial u_j'}{\partial x_j}} + \frac{\partial}{\partial x_j}\overline{\left(u_j'\frac{1}{2}u_i'u_i'\right)} + \frac{1}{Re}\frac{\partial^2}{\partial x_j^2}\left(\frac{1}{2}\overline{u_i'u_i'}\right)$$

$$-\frac{\partial}{\partial x_j}\overline{p'\delta_{ij}u_j'} + \underbrace{\overline{\left(-<u_i'u_j'>\right)\frac{\partial \tilde{u}_i}{\partial x_j}}}_{P_{EHD}} - \underbrace{\overline{\tilde{u}_j\frac{\partial}{\partial x_j}<\frac{1}{2}u_i'u_i'>}}_{T_{EHD}} \quad . \tag{24}$$

The terms on the r.h.s. represent: production by mean flow, dissipation, pressure-strain correlation, turbulent diffusion, viscous diffusion, pressure diffusion, production by EHD flows (P_{EHD}) and transport by EHD flows (T_{EHD}) respectively. In the absence of EHD flows – i.e. in turbulent channel flow – the last two terms are obviously zero. The third, fourth, fifth, sixth and eighth terms contribute to the energy transfer to other flow regions, and their integral over the flow domain is zero. Production by the mean flow, and by EHD flows, are the energy gain terms, and dissipation is the energy loss term. All terms included in Eq. 24 are normalized by u_τ^4/ν and are shown in Figure 18, except for the pressure-strain term. For clarity of presentation, the EHD-related terms, P_{EHD} and T_{EHD}, have been plotted by shifting their zero by -0.2 and -0.3, in the low and high N_{EHD} cases, respectively. Turbulence production by action of the mean flow is given by the product of the mean strain rate, $\mathrm{d}\overline{u}/\mathrm{d}z$, shown in Figure 19, and $-\overline{u'w'}$, the turbulent Reynolds stress, as shown in Figure 15. Note that the Reynolds stresses decrease with increasing N_{EHD}, consistent with the mean velocity increase with increasing N_{EHD} discussed earlier. For the N_{EHD} examined, mean flow production is slightly increased by the presence of EHD flows. Consider now the new term of turbulence production by EHD flows: P_{EHD} is given by the action of the phase-averaged fluctuating Reynolds stress, $-<u_i'u_j'>$, against the organized strain rate, $\partial\tilde{u}_i/\partial x_j$. In the low N_{EHD} case, this term accounts for one fourth of total turbulence kinetic energy production, whereas in the high N_{EHD} case it has the same importance as the mean flow production term. Since $\tilde{u}_2 = \partial\tilde{u}_i/\partial x_2 = 0$, P_{EHD} may be written as:

$$P_{EHD} = -\overline{<u_1'u_1'>\frac{\partial\tilde{u}_1}{\partial x_1}} - \overline{<u_1'u_3'>\frac{\partial\tilde{u}_1}{\partial x_3}} - \overline{<u_3'u_1'>\frac{\partial\tilde{u}_3}{\partial x_1}} - \overline{<u_3'u_3'>\frac{\partial\tilde{u}_3}{\partial x_3}} \quad , \tag{25}$$

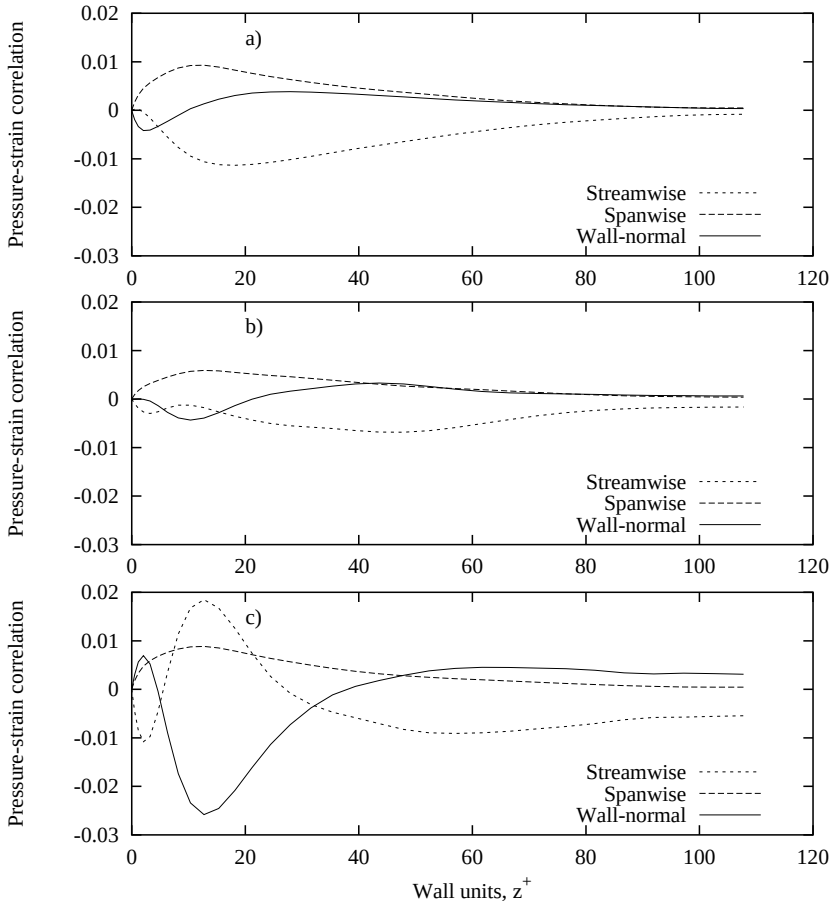

Figure 20. Profile of pressure-strain correlation for a) channel flow; b) low N_{EHD}; c) high N_{EHD}. In channel flow, turbulence kinetic energy is produced entirely in the streamwise direction. EHD flows produce turbulent kinetic energy both in wall-normal and in streamwise directions.

from which we see that turbulence kinetic energy is produced both in the streamwise and in the wall-normal direction. From Figures 18 b) and c), it may be observed that turbulence is produced mostly in the wall region. Production in the wire region is very limited. Furthermore, increasing the intensity of EHD flows displaces the peak toward the wall. Eq. 25 shows that no turbulence production occurs in the spanwise component, which thus receives kinetic energy from the pressure-strain terms, which are shown in Figure 20.

For incompressible fluids the sum of the three pressure-strain components is always zero. Examination of each component, however, indicates how kinetic energy is transferred across the velocity components. In channel flow turbulence kinetic energy is received entirely by the streamwise component, and is redistributed to the other components. The wall-normal component becomes negative at the wall because fluctuations are damped. EHD flows modify this bal-

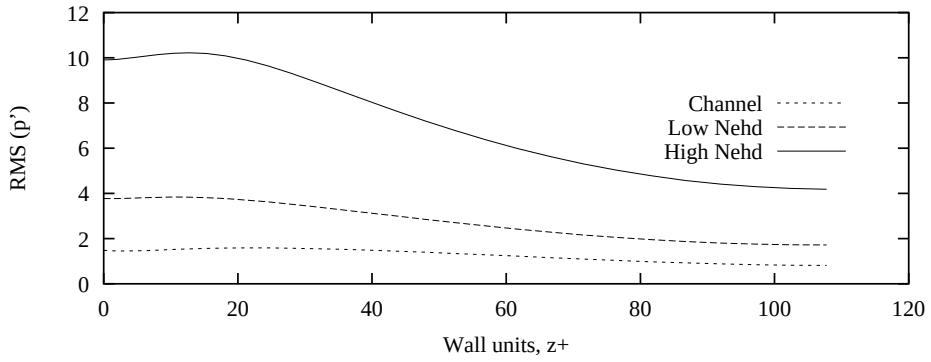

Figure 21. Profile of the RMS pressure fluctuations in channel flow, low N_{EHD}, and high N_{EHD} cases.

ance producing $1/2\overline{u_3'^2}$ at the edge of the wall region (around $z^+ \simeq 10$) and $1/2\overline{u_1'^2}$ at the wall. Finally, we can see that in the low N_{EHD} case, all pressure-strain terms are decreased. Since it can be seen from Figure 21 that the RMS of pressure fluctuations increases due to the EHD flows, it can be concluded that turbulence velocity gradients are also reduced, corresponding to a general *smoothing* of the field. It is apparent that EHD flows increase turbulence production. However, they also increase dissipation. The peak at the wall almost doubles in the low N_{EHD} case, and increases more than three times in the high N_{EHD} case. Turbulent diffusion, viscous diffusion and pressure diffusion are also affected by the presence of EHD flows. Finally the EHD flows transfer term, T_{EHD}, redistributes turbulence kinetic energy to other regions by means of the organized flows. Its most significant role is to receive energy in the wall region and redistribute it farther from the wall.

6 Forcing Turbulence with Streamwise EHD Flows

In the previous section, we examined the structure of the boundary layer and we set up a methodology to investigate the complex flow field generated by the interactions among the EHD flows and the channel flow.

In this section, we will examine the influence of streamwise-independent standing waves, or rather, of large-scale vortical flows. Specifically, we will examine the modification of a turbulent Poiseuille flow due to large-scale, streamwise electrohydrodynamic (EHD) structures which are generated by high-potential, streamwise wires in the middle of the duct. As shown in Figure 1, this may be a possible, new configuration for ESPs if large drag reduction could be found, since the pressure drop can be a significant parameter for optimization of operative costs. In this work, we considered a first possibility which is precisely switching the flow direction. Compared to the usual configuration for ESPs, only the orientation of EHD flows with respect to the mean flow changes. The size of EHD flows is the same. Thus, there are ample margins for optimization. Previous investigations (Soldati, 2000) suggest that this change in the flow direction would scarcely affect particle collection efficiency in an ESP. Furthermore, in the light of recent experimental

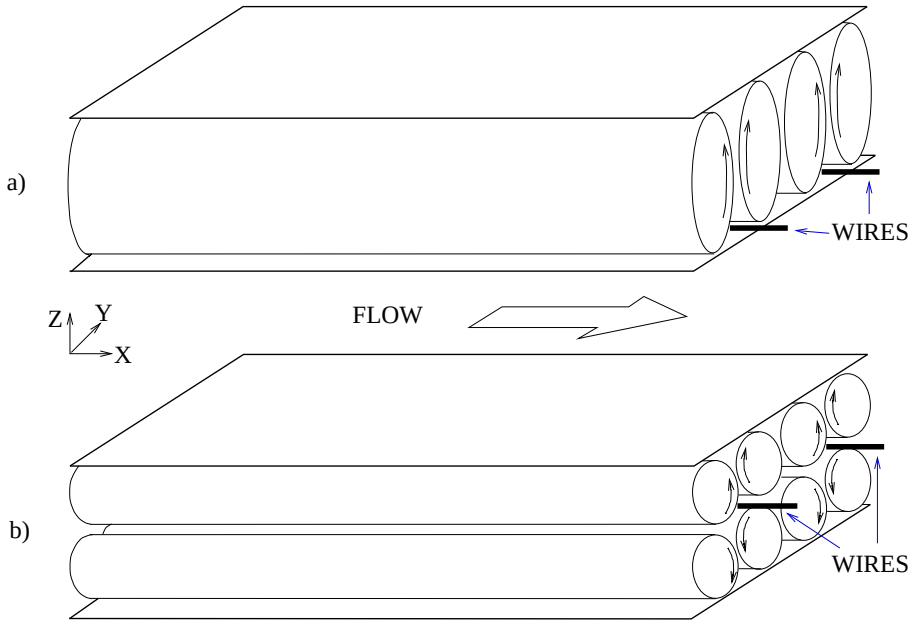

Figure 22. Diagram of the control flows: a) E-control: streamwise vortical structures generated by wires embedded in one wall; b) C-control: streamwise vortical structures generated by wires placed in the middle of the channel. In both cases, there is no through-flow.

results (Roth et al., 1998, Roth et al. 2000, Artana et al., 2001), the strategy proposed in this paper could also be exploited in other industrial fields.

We considered two types of control flows: $i)$ two-dimensional jets issuing from one wall and impinging on the other, aligned in the streamwise direction (*E-control*); $ii)$ two-dimensional jets issuing from the center of the channel, also aligned in the streamwise direction (*C-control*). A schematic of the two configurations is given in Figure 22 with the position of the wires in order to compare the vortical structures to those generated by spanwise wires as in Figure 1. The C-control configuration may be obtained easily from a technological viewpoint just by switching the direction of the mean flow through the ESP duct by 90^o. The E-control configuration may be obtained by inserting a non-conductive plate in the plane of the wires and by switching the direction of the mean flow through the ESP duct by 90^o. The streamwise control flows are such that they do not produce a net flow throughput, but are meant to force spanwise the boundary layer, thus modifying turbulent transfer mechanisms at the wall, which are responsible for drag production. All simulations started from a channel flow simulation, with no EHD flows calculated for a shear Reynolds number $Re_\tau = 108$ over a grid of $64 \times 64 \times 65$ (Soldati et al., 1993). The body force is then applied and simulations run until a new steady state is reached. The wires are kept at a potential of $15\,000\,V$ for all simulations $-$a potential typical in ESP applications $-$while the current flowing through the duct is varied. This allows control flows of different intensities.

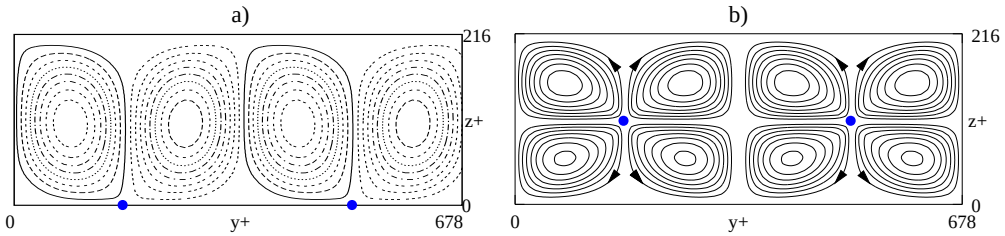

Figure 23. Streamlines of the control flows: a) E-control: streamwise vortical structures generated by wires (represented by blue dots) embedded in one wall; contours go from -130 to 130 with increments of 15 in wall units; b) C-control, with streamwise wires (represented by blue dots) in the middle of channel; contours go from -35 to 35 with increments of 4 in wall units.

After the steady state is reached, simulations are continued for a sufficient number of time steps to obtain adequate statistics (see Fulgosi, 1998, for details).

The control variable in this type of flow control is the intensity of the electric current flowing through the duct. Thus, we could use, as in the previous case, the N_{EHD} defined in Equation 11, which is proportional to the electric current. However, this information is not directly related to the structure of the turbulence field, and the organized control-flow flowrate should be used in order to make comparison with previous works (Schoppa and Hussain, 1998) and other types of body forces generating control flows (Du and Karniadakis, 2000). It is not easy to predict a-priori the intensity and the shape of the control flows once they have been interacting with the turbulent through-flow. We characterized the control flows on the basis of the shape and intensity they assumed in a no-through flow case. Since in this case there is no applied pressure gradient and, consequently, there is no net flow through the duct, we calculated the flowrate of each convective EHD cell. In Figure 23 a) and b), the streamlines of the flow field obtained for a zero pressure gradient are shown for one of the E cases and one of the C cases respectively. The position of the wires is identified with the blue dots and in all cases, the wire-electrodes have a spanwise spacing of 340 wall units. The flow structures are two-dimensional and reflect the distribution of the body force. Current intensity and the corresponding flowrates for the seven cases investigated are reported in Table 1. The flowrates are normalized by the flowrate of the channel with no imposed flow.

Table 1. SUMMARY OF THE SIMULATIONS

	Current Density (A/m^2)	$W_{control}/W_{channel}$ (%)
E1	1.50E-05	12.7
E2	2.00E-05	17.4
E3	5.00E-05	48.5
C1	1.00E-07	2.7
C2	5.00E-06	8.3
C3	2.00E-05	25.2
C4	5.00E-05	58.9

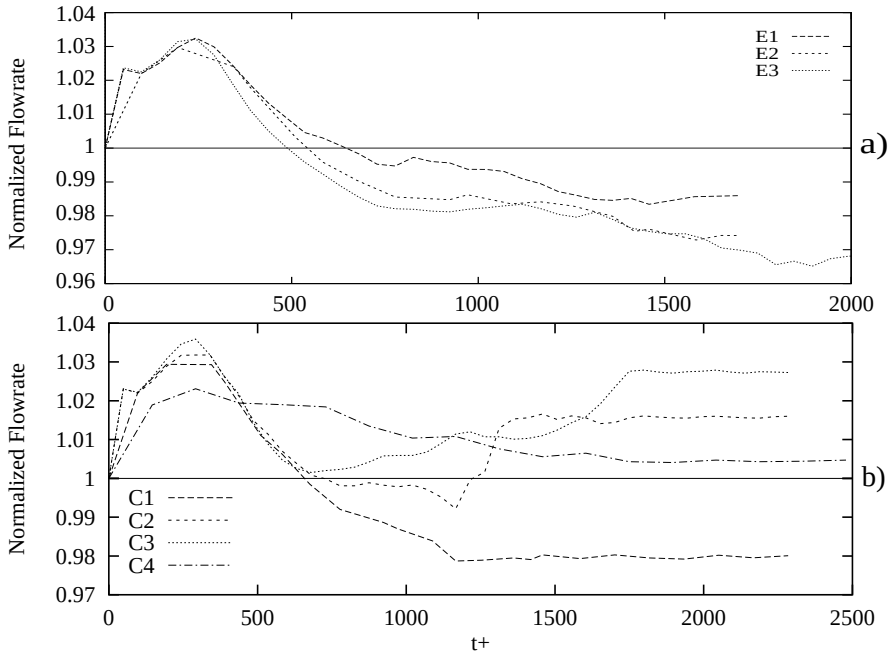

Figure 24. Time evolution of flowrate; a) E-control, b) C-control. Flowrates are normalized by unforced channel flowrate. Initial increase is followed by a steady state. In all E-control cases, flowrate is lower than the corresponding channel flowrate. In the C-control, an increase of flowrate is obtained for the three simulations with higher intensity of the body force.

6.1 Overall Drag Modification

Since the pressure drop is maintained the same for all simulations, all drag changes are indicated by the behavior of the flowrate. Drag reduction is indicated by an increase of the flowrate and drag increase is indicated by a decrease of the flowrate. In Figures 24 a) and b), the time-behavior of the flowrate normalized by the unforced case flowrate is shown for the different E cases and C cases respectively. In the present application, we are interested in the steady-state. We notice, however, that after induction of EHD flows, there is a transient lasting about 600 dimensionless time units in which the mean velocity increases for all simulations. The behavior of non-equilibrium three-dimensional boundary layers, such as the one investigated in the present case, is not well understood yet (Coleman et al., 1996), and, at present, we have no sound explanation for the transient behavior of the mean flowrate, which is also associated to a transient increase in the wall drag (not shown here). Considering the E-control flow cases (Figure 24 a)), all simulations attain a steady state in which the velocity is lower than the corresponding uncontrolled flow case. Variations are, in any case, modest, with a maximum decrease of about 3% in case E3, in which the control flows are strongest. Drag behavior with the intensity of the EHD flows is monotonic, suggesting that this configuration may not be optimized for drag reduction. The application of C-control flows gives a more complex behavior of the overall drag with the

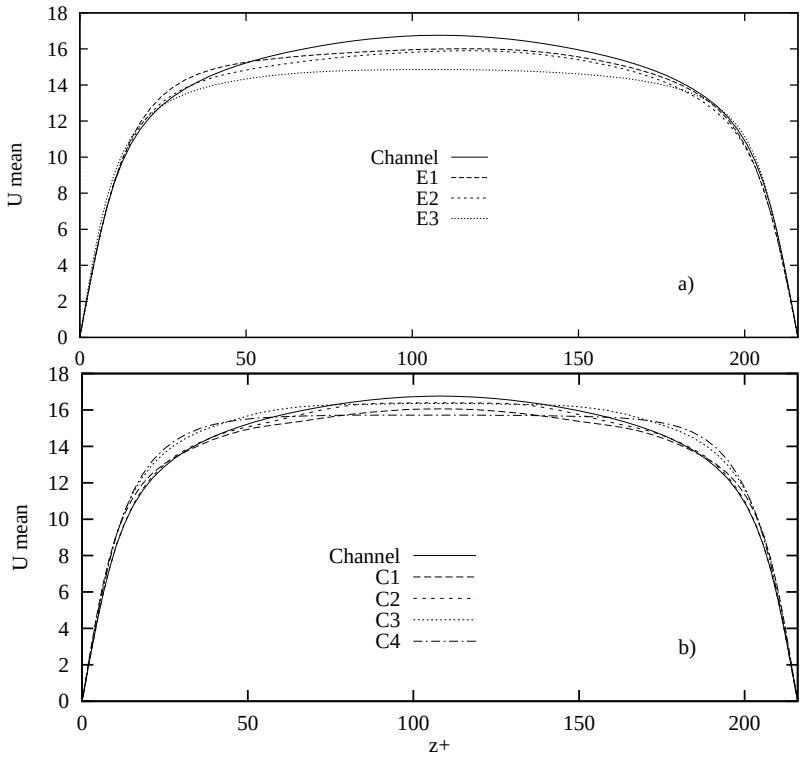

Figure 25. Behavior of the mean velocity profile for a) E-control, and b) C-control for all simulated cases, compared with velocity profile of unforced channel flow case.

intensity of the control flows: at very low intensity, drag is increased, whereas for higher intensity drag is reduced. In cases C2 and C3 the mean velocity reaches a steady state with increases of 2% and 3% respectively. In case C4, the initial peak is lower and the slope toward the steady state is milder. A steady state is reached after about 1500 wall time units with practically no drag reduction compared to the unforced case. Thus, maximum drag reduction seems to exist for this type of forcing flows - conditions close to case C3.

6.2 Mean Velocity and Turbulence Intensity

The mean velocity profile for the unforced channel-flow case is compared against the mean velocity profiles of the forced cases in Figures 25 a) and 25 b) for the E control cases and the C control cases respectively. In the E-control cases, all the profiles appear flattened in the center of the channel. Also in the C-control cases, the profiles appear flattened in the center of the channel but increase in the wall region, producing, in the three higher-potential cases, a net increase in the flowrate, as indicated by Figure 24. In the present simulations, energy is fed into the turbulence field by the mean pressure gradient and by the electrostatic forces. A careful examination of turbulence statistics, turbulence structure and energy and Reynolds stress budgets is advisable in

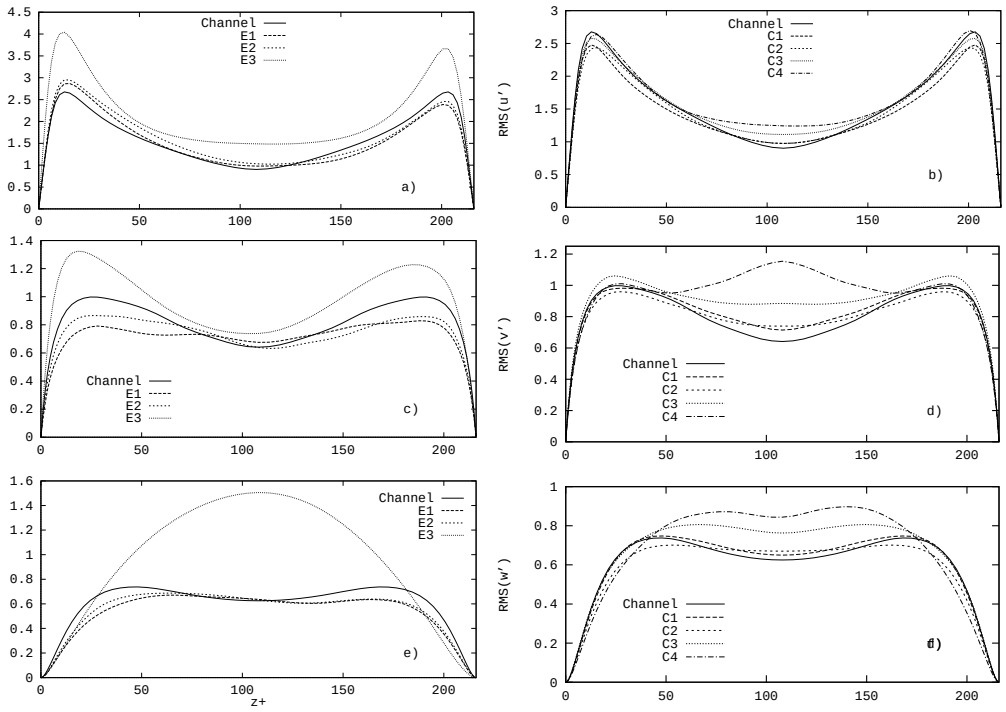

Figure 26. Variance of velocity fluctuations for a), c), e) E-control cases, and b), d), f) C-control cases, compared with turbulence intensity of the unforced channel flow case.

order to establish the effects EHD flows have on the turbulence field and on the mean field. To do this analysis, a suitable method of filtering out the large-scale forcing flows should be adopted. The electrostatic field is two-dimensional and a filtering procedure could be averaging over the x direction, as we have done in Section 5.2. However, the streamwise EHD vortical flows have sizes comparable to those of the streamwise vortices typical of the boundary layer, with which they interact in a complex way. In practice, and in particular for the C-control cases, the EHD vortices have a size of about 108 wall units, whereas the quasi-streamwise vortices, on which we would like to focus, have a size typically up to 40 wall units. In the cases of lower intensity of EHD flows, the EHD flows themselves are not steady because they are perturbated by the quasi-streamwise vortical flows. Thus, averaging over the streamwise direction (Soldati and Banerjee, 1998) allows identification of EHD flows only when they are much stronger than unforced case vortices - i.e. in case C4, which altogheter is not representative for all the other cases.

In Figures 26 a) and 26 b), we show turbulence intensity in the streamwise direction, which is not directly modified by the EHD flows, since they have a null component in the x direction only. For E-control cases, turbulence intensity appears increased close to the wall from which the jets issue, i.e. the one with the embedded wires, and decreased close to the other wall for all cases with the exception of case E3, in which large turbulence intensity is observed throughout the channel. In all cases, however, the increase of the intensity of control flows produces a

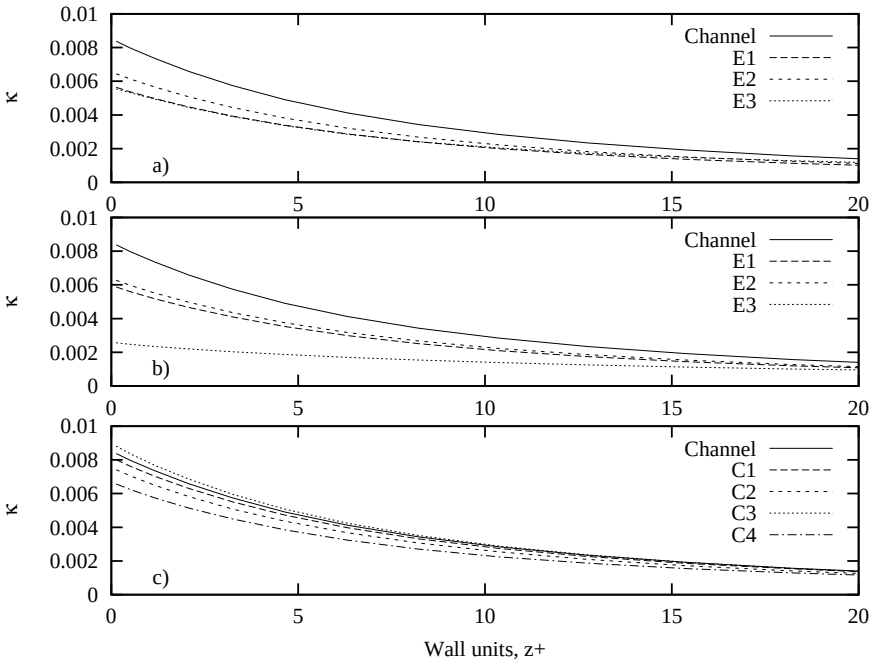

Figure 27. EHD flows effect on the wall mass transfer coefficient, κ, in turn connected to the behavior on the near-wall normal velocity fluctuations. First, the effect both at the wall with embedded wires, a), and at the wireless wall, b), is shown for all E-control cases. Second, the effect at the wall is shown for all C-control cases, c).

monotonic trend in the modification of turbulence intensity. In all C-control cases, turbulence intensity decreases in the wall region and increases in the central region of the channel. Compared to the unforced channel-flow case, for increasing intensity of the control flows, there is an initial decrease of turbulence intensity in the wall region −cases C1 and C2 −followed by an increase in turbulence intensity in cases C3 and C4. This indicates that after initially damping turbulence production, higher intensity control flows increase turbulence levels, producing turbulence by their own mechanisms (Soldati and Banerjee, 1998). The peak in the unforced case is always larger than in the forced cases. Turbulence intensity profiles in spanwise and wall-normal directions are also shown in Figures 26 c), d) and 26 e), f) respectively. Their behavior is influenced by the fluctuations of both the electrostatic field and the unforced channel vortical structures. Thus, an analysis of such profiles is not useful to educe how the turbulent field is affected by EHD flows, except for case C4 as mentioned above.

6.3 Influence on Mass Transfer at the Wall

As discussed in the previous sections, mass transfer at the wall is influenced by the modulation of the quadrant events. In Figures 27 a), b) and c), the behavior of the function $\overline{\kappa^2}$ is presented for E-control cases and C-control cases. The behavior for unforced channel flow case is also

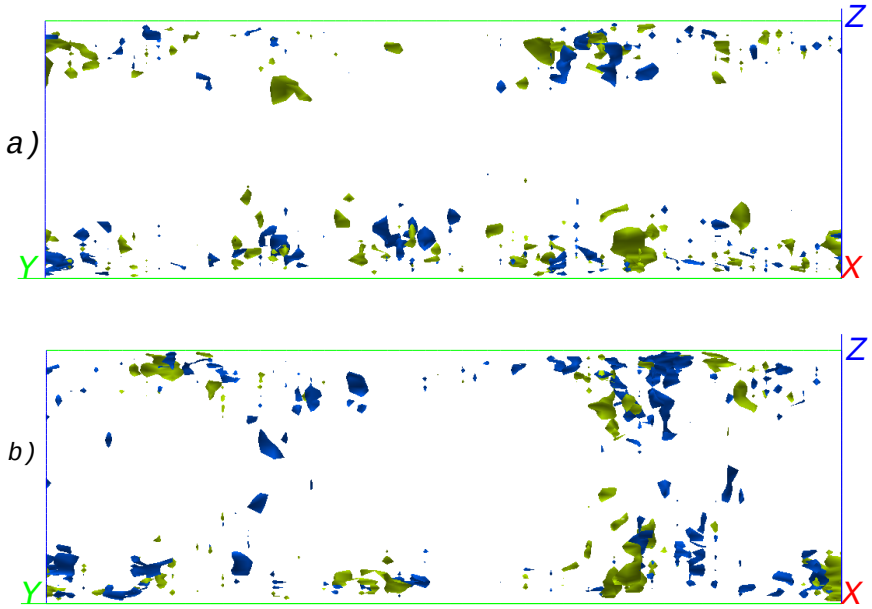

Figure 28. a) Front view of quasi-streamwise vortices in channel flow; b) front view of quasi-streamwise vortices in C-4 case. Blue regions indicate clockwise rotation; green regions indicate counter clockwise rotation.

reported for comparison purposes. As can be observed from Figure 26, turbulence intensity in the wall-normal direction is damped with respect to the unforced channel flow case in the E-cases. This suggests that such type of forcing flows act to reduce the turbulent mass transfer at the solid wall, as confirmed in Figure 27 a), where the effect of EHD forcing flows on $\overline{\kappa^2}$ is shown at the wall with embedded wires. The same conclusion may be drawn at the wireless wall (Figure 27 b)): in all E-control cases and particularly in case E3, a net mass transfer reduction is obtained. When a C-control is applied, the gradient of wall-normal velocity fluctuations appears increased close to the wall only in case C3, being decreased in all other cases (see Figure 26). Thus, from Figure 27 c), we can observe that mass transfer at the wall increases only in case C3, being reduced in all other cases.

6.4 Modulation of the Distribution of Quasi-Streamwise Vortices

As discussed previously, a careful and insightful examination of turbulence structure at the wall in the EHD forced cases would require a filtering of the almost steady EHD vortical flows. This is not easy, since the size of the vortical flows is comparable to that of the structures we want to examine – i.e. the quasi-streamwise vortices. However, this filtering may be performed following the strategy exploited in the spanwise forcing flow case C4 (Marchioli, 1999), in which the forcing flows are by far more coherent that quasi-streamwise vortices. In Figure 28 a), a front view of isosurfaces of the streamwise component of Ω, Ω_1, is shown for the whole computational

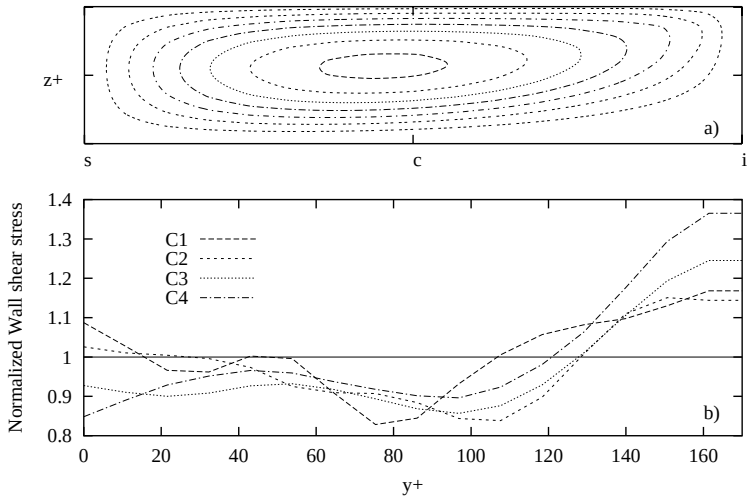

Figure 29. Influence of single EHD streamwise vortex on time-averaged wall shear-stress. a) Undisturbed (no-through flow case) EHD vortex; b) time-average of wall shear-stress in each case normalized by time-average of wall shear-stress in unforced channel case.

domain. Quasi-streamwise vortices are generated at the wall and are present in the region where the shear is higher, close to the walls (Lam and Banerjee, 1992). We performed the same analysis for the C4 case with the mean and EHD forced components filtered out, leaving only the fluctuating turbulent velocity field. The isosurfaces of Ω_1 are shown in Figure 28 b). It is seen that streamwise vortices seem to be localized close to the walls and in the regions of the wall-directed jets −i.e. where the shear stress is high enough. They are absent in the regions characterized by the EHD backflows from the wall.

6.5 Wall Shear Stress and Impinging EHD Jets: Local drag Reduction/Increase

In their paper on the dynamics of wall coherent structures, Schoppa and Hussain (1997) suggest that lateral forcing would be appropriate to reduce drag by damping the streak-regeneration mechanism. In their subsequent letter (Schoppa and Hussain, 1998), they exploit large, mathematical vortices with streamwise axis and they analyze the influence these vortices have on turbulence in a specific way which we followed (Fulgosi et al., 1999, Soldati, 2000c) and present here to extrapolate an ideal forcing EHD flow.

Consider Figure 29 a), where one single EHD-generated vortex is shown: the EHD jet impinges on the wall at “i”, then the streamlines run parallel to the wall through “c” and they return toward the outer flow at “s”. In Figure 29 b), the behavior of the normalized, time-averaged wall shear-stress is shown for each simulation. In all forced cases, the time-averaged wall shear-stress increases in the impingement region and decreases where the EHD flow streamlines are parallel to the wall. In the lower intensity cases, C1 and C2, the wall shear-stress increases again close to point “s”. Following the definition of Schoppa and Hussain (1998), we can name the “i-s” region

in Figure 29 a) as vortex forcing and the "c-s" region in Figure 29 a) as wall-jet forcing. In case C4, the time-averaged wall shear-stress in the "c-s" region is about 90% of that in the unforced case. In case C3, which is the most favorable, the time-averaged wall shear-stress in the "c-s" region is about 87% of that in the unforced case. Apparently, wall shear-stress is significantly reduced in the region where the forcing flow is parallel to the wall −as suggested by Schoppa and Hussain (1997) - but it is greatly increased in the region where extra drag is generated by the EHD jet impinging on the wall. This increase is, in most cases, sufficient to reduce the beneficial effect to a few percent drag reduction.

7 Concluding Remarks and Future Developments

In this work, we tried to examine possible develpoments of turbulence control in boundary layers by using large-scale EHD flows. This work may have relevance in Electrostatic Precipitators and, being of fundamental nature, in a number of other applications. We discussed the possible mechanisms which control turbulence structure in the boundary layer and we hypotesized a possible strategy to control them. Specifically, we have been inspired by the works of Schoppa and Hussain (1997, 1998) who concluded that a suitable large-scale spanwise forcing could stabilize turbulent structures and damp turbulence in boundary layers.

The application we have in mind is Electrostatic Precipitation. We presented results relative to turbulence modifications in ESPs owing to the spanwise EHD flows occurring in the usual configuration. For this geometry, we discussed thoroughly the numerical methodology exploited and the concept of triple decomposition (Hussain, 1983), which helps in identifying the energy fluxes among the mean field, the EHD flows field and the turbulence field. Considering also that, from the particle collection viewpoint (Soldati, 2000a) EHD flows do not appear to have a large impact, we examined a new geometry for EHD flows: we considered the standard ESP geometry except that the wires are now parallel to the mean flow. If a suitable geometrical configuration could be found in which EHD flows have a positive effect on drag reduction and on particle collection efficiency, operative costs could be reduced. In this work, we examined just one single geometry, namely the standard geometry, but considered the wires parallel to the flow rather than transverse to the flow. From the particle collection viewpoint, this change is presumed negligible (Soldati, 2000). From the drag reduction viewpoint it could present interesting developments.

From the numerical simulations performed, it appears that EHD-induced, streamwise vortical flows may be used to modify turbulence characteristics even though they did not lead to dramatic changes in drag in the specific configuration we examined, which is of interest for ESP design. Specifically, we found that the wire-to-wire distance is too small for drag reduction purposes, and the part of the EHD flow which is parallel to the wall −drag reducing part −is marginally sufficient to compensate the drag increase effects of the EHD jets impinging on the wall.

In particular, we confirmed ideas developed in previous works (Schoppa and Hussain, 1998) in which the forcing flows were synthetic flows −i.e. not corresponding to physical mechanisms but simply mathematical expressions −and we found trends similar to those found by Du and Karniadakis (2000) even though with much less dramatic drag reduction because of the specific geometry of the forcing flows, which are not optimized. However, we believe that, if the mechanisms of the wall-parallel jet drag reduction could be exploited, the advantages of the configuration we propose could be significant.

At present we are trying to devise a numerical strategy for optimizing the distribution of the electrostatic field in order to maximize drag reduction. This strategy is based first on deriving a low-order model for the turbulence flow field including the presence of forcing EHD flows (Beux et al., 2000a, 2000b). Second, from the current distribution which is optimal for drag reduction, we will reconstruct the solution of the original Maxwell problem in order to derive operative parameters.

Acknowledgment

The authors would like to thank Marco Fulgosi, now at ETH, Zurich, for performing some calculations. Computational resources provided by ENEL/CRT, Pisa, Italy on their CRAY T94/164 are gratefully acknowledged.

References

Artana, G., D'Adamo, J., Legert, L., Moreau, E., and Touchard, G. (2001). Flow control with electrohydrodynamic actuators. *AIAA 2001-0351 39th Aerospace Sciences Meeting*, January 8-11, 2001, Reno (NV).

Baron, A., and Quadrio, M. (1995). Turbulent drag reduction by spanwise wall oscillations. *Applied Scientific Research*, **4**, 311–326.

Bernstein, S., and Crowe, C. T. (1981). Interaction of electrostatics and fluid dynamics in electrostatic precipitators. *Environment International*, **6**, 181–200.

Beux, F., Iollo, A., Salvetti, M. V., and Soldati, A. (2000). A POD approach for turbulent flow control by electro-hydrodynamic large-scale structures. *ECCOMASS 2000, European Congress on Computational Methods in Applied Sciences and Engineering*, Barcelona, Spain, Sept. 11-14, 2000.

Beux, F., Iollo, A., Salvetti, M. V., and Soldati, A. (2000). Approximation and reconstruction of the electrostatic field in wire-plate precipitators by a low-order model. *Journal of Computational Physics*, (Submitted).

Bonnet, J. P., and Delville, J. (1996). General concepts on structure identification. In Bonnet, J. P., ed., *Eddy Structure Identification*, Springer-Verlag, Wien, 1–59.

Bonnet, J. P., Delville, J., Glauser, M. N., Antonia, R. A., Bisset, D. K., Cole, D. R., Fiedler, H. E., Garem, J. H., Hilberg, D., Jeong, J., Kevlahan, N. K. R., Ukeiley, L. S., and Vicendeau, E. (1998). Collaborative testing of eddy structure identification methods in free turbulent shear flows. *Experiments in Fluids*, **25**, 197–225.

Brooke, J. W., and Hanratty, T. J. (1993). Origin of turbulence-producing eddies in a channel flow. *Physics of Fluids*, **5**, 1011–1022.

Campbell, J. A., and Hanratty, T. J. (1983). Mechanisms of turbulent mass transfer at a solid boundary. *AIChE Journal*, **29**, 221.

Choi, K.-S. (2001). Turbulent drag reduction mechanisms: strategies for turbulence management. In this book.

Choi, K.-S., and Graham, M. (1998). Drag reduction of turbulent pipe flows by circular-wall oscillation. *Physics of Fluids*, **10**, 7–9.

Choi, K.-S., and Clayton, B. R. (2001). The mechanism of turbulent drag reduction with wall oscillation. *International Journal of Heat and Fluid Flow*, **22**, 1-9.

Chong, M. S., Perry, A., and Cantwell, B. J. (1990). A general classification of three-dimensional flow fields. *Physics of Fluids A*, **2**, 765–777.

Coleman, G. N., Kim, J., and Le, A. T. (1996). A numerical study of three-dimensional bounded flows. *International Journal of Heat and Fluid Flow*, **17**, 333–342.

Crawford, C. H., and Karniadakis, G. E. (1997). Reynolds stress analysis of EMHD-controlled wall turbulence. Part I. Streamwise forcing. *Physics of Fluids*, **9**, 788–804.

Davidson, J. H., and Shaughnessy, E. J. (1986). Turbulence generation by electric body forces. *Experiments in Fluids*, **4**, 17–43.

Davidson, J. H., and McKinney, P. J. (1989). Turbulent mixing in a barbed plate-to-plate electrostatic precipitator. *Atmospheric Environment*, **23**, 2093–2150.

Davidson, J. H., and McKinney, P. J. (1991). EHD flow visualization in the wire-plate and barbed plate electrostatic precipitator. *IEEE Transactions Industrial Applications*, **27**, 154–180.

De Angelis, V., Lombardi, P., Andreussi, P., and Banerjee, S. (1997). Mycrophysics of scalar transfer at air-water interfaces. Invited Paper, IMA Conference on *Wind over Wave Couplings*, Salford, UK, 8-10 April, 1997, Oxford University Press.

Dinelli, G., and Rea, M. (1990). Pulse power electrostatic technologies for the control of flue gas emission. *Journal of Electrostatics*, **25**, 23–40.

Dinelli, G., Civitano, L., and Rea, M. (1991). Industrial experiments on pulse corona simultaneous removal of NO_X and SO_2 from flue gas. *IEEE Transactions on Industry Applications*, **26**, 535–541.

Du, Y., and Karniadakis, G. E. (2000). Suppressing wall turbulence by means of a transverse traveling wave. *Science*, **288**, 1230–1234.

Dubief, Y., and Delcayre, F. (2000). On coherent-vortex identification in turbulence. *Journal of Turbulence*, **1**, 11–32. Retrieved at `http://jot.iop.org`.

Fulgosi, M. (1998). *Strategies to control turbulent boundary layers by large-scale EHD structures*. MS Thesis, University of Udine (In Italian).

Fulgosi, M., Banerjee, S., and Soldati, A. (1999). Turbulence modulation by an array of large-scale streamwise structures of EHD origin. *ASME Paper No. FEDSM99-6934, 3rd ASME/JSME Fluids Engineering Conference*, San Francisco, CA, July, 18-22, 1999.

Fulgosi, M., Marchioli, C., and Soldati, A. (2000). Turbulent drag reduction by streamwise EHD flows: a new configuration for electrostatic precipitators. *Proceedings of the 2nd International Workshop on Electrical Conduction, Convection and Breakdown in Fluids*, Grenoble (France), May, 5, 2000, 139–142.

Harris, J. A., and Street, R. L. (1994). Numerical simulation of turbulent flow over a moving wavy boundary: Norris and Reynolds extended. *Physics of Fluids*, **6**, 924–943.

Hunt, J. C. R. (1995). Effects of body forces on turbulence. In Benzi, R., ed., *Advances in Turbulence V*. Kluwer, Dordrecht (NL), 229–250.

Hunt, J. C. R., Wray, A. A., and Moin, P. (1998). Eddies, stream and covergence zones in turbulent flows. *Center of Turbulence Research Rep*., CTR-S88, 193.

Hussain, F. (1983). Coherent structures – reality and myth. *Physics of Fluids*, **26**, 2816–2838.

Jeong, J., and Hussain, F. (1995). On the identification of a vortex. *Journal of Fluid Mechanics*, **285**, 69–83.

Jeong, J., Hussain, F., Schoppa, W., and Kim, J. (1997). Coherent structures near the wall in a turbulent channel flow. *Journal of Fluid Mechanics*, **322**, 185–202.

Jimenez, J., and Moin, P. (1991). The minimal flow unit in near-wall turbulence. *Journal of Fluid Mechanics*, **225**, 213–233.

Jimenez, J., and Pinelli, A. (1999). The autonomous cycle of near-wall turbulence. *Journal of Fluid Mechanics*, **389**, 335–359.

Jung, W., Mangiavacchi, N., and Akhavan, R. (1992). Suppression of turbulence in wall-bounded flows by high frequency spanwise oscillations. *Physics of Fluids A*, **4**, 1605–1607.

Kallio, G. A., and Stock, D. E. (1986). Computation of electrical conditions inside wire-duct electrostatic precipitators using a combined finite-element, finite-difference technique. *Journal of Applied Physics*, **59**, 1799–1806.

Kallio, G. A., and Stock, D. E. (1992). Interaction of electrostatic and fluid dynamic fields in wire-plate electrostatic precipitators. *Journal of Fluid Mechanics*, **240**, 133–153.

Kasagi, N., and Iida, O. (1999). Progress in direct numerical simulation of turbulent heat transfer. Keynote Paper, *5th ASME/JSME Joint Thermal Engineering Conference*, San Diego, CD-ROM Publication, ASME, March, 1999.

Kasagi, N., and Ohtsubo, Y. (1993). Direct numerical simulation of low Prandtl number thermal field in a turbulent channel flow. In Durst, F., Friedrich, R., Launder, B. E., Schmidt, F. W., Schumann, U., and Whitelaw, J. H., eds., *Proceedings of the 8th Symposium on Turbulent Shear Flows*, Springer-Verlag, Berlin, 1993, 97-119.

Kelly-Wintenberg, K., Montie, T. C., Brickman, C., Roth, J. R., Carr, A. K., Sorge, K., Wadsworth, L. C., and Tsai, P. P. Y. (1998). Room temperature sterilization of surfaces and fabrics with a one atmosphere uniform glow discharge plasma. *Journal of Industrial Microbiology and Biotechnology*, **20**, 69-74.

Kim, J., and Hussain, F. (1993). Propagation velocity of perturbations in turbulent channel flow. *Physics of Fluids A*, **5**, 695–706.

Kim, J., Moin, P., and Moser, R. (1987). Turbulence statistics in fully developed channel flow at low Reynolds number. *Journal of Fluid Mechanics*, **177**, 133–166.

Kline, S. J., Reynolds, W. C., Schraub, F. A., and Runstadler, P. W. (1967). The structure of turbulent boundary layer. *Journal of Fluid Mechanics*, **70**, 741–773.

Kline, S. J., and Robinson, S. K. (1990). Quasi-coherent structures in the turbulent boundary layer:Part 1.Status report on community-wide survey of the data. In Kline, S. J., Afgan, N. H., eds., *Near-Wall Turbulence*. Hemisphere, New York.

Lai, F. C., McKinney, P. J., and Davidson, J. H. (1995). Oscillatory electrohydrodynamic gas flows. *Journal of Fluids Engineering*, **117**, 491–500.

Lam, K., and Banerjee, S. (1992). On the condition of streak formation in bounded flows. *Physics of Fluids A*, **4**, 306–320.

Leonard, G. L., Mitchner, M., and Self, S. A. (1983). An experimental study of the electrohydrodynamic flow in electrostatic precipitators. *Journal of Fluid Mechanics*, **127**, 123–145.

Leutert, G., and Bohlen, B. (1972). The spatial trend of electric field strength and space charge density in plate type electrostatic precipitator. *Staub Reinhalt Luft*, **32**, 27–34 (In English).

Lombardi, P., De Angelis, V., and Banerjee, S. (1996). Direct numerical simulation of the near-interface turbulence in coupled gas-liquid flow. *Physics of Fluids*, **8**, 1643–1665.

Malik, M. R., Weinstein, L. M., and Hussaini, M. Y. (1983). Ion wind drag reduction. *AIAA 83-0231, 21th Aerospace Sciences Meeting*, January 10-13, 1983, Reno (NV).

Marchioli, C. (1999). *Turbulent transfer mechanisms near the wall*. MS Thesis, University of Udine (In Italian).

Massines, F., Rabehi, A., Decomps, P., Gadri, R. B., Segur, P., and Mayoux, C. (1998). Experimental and theoretical study of a glow discharge at atmospheric pressure controlled by dielectric barrier. *Journal of Applied Physics*, **83**, 2950–2957.

Mc Daniel, E. W., and Mason, E. A. (1973). *The mobility and diffusion of ions in gases*. New York, NY, Wiley.

Montie, T. C., Kelly-Wintenberg, K., and Roth, JR. (2000). An overview of research using the one atmosphere uniform glow discharge plasma (OAUGDP) for sterilization of surfaces and materials. *IEEE Transactions on Plasma Science*, **28**, 41-50.

Ohadi, M. M., Nelson, D. A., and Zia, S. (1991). Heat transfer enhancement of laminar and turbulent pipe flow via corona discharge. *International Journal of Heat and Mass Transfer*, **34**, 1175–1187.

Owsenek, B. L., Seyed-Yagoobi, J., and Page, R. H. (1995). Experimental investigation of corona wind heat transfer enhancement with a heated horizontal flat plate. *ASME Journal of Heat Transfer*, **117**, 309–315.

Owsenek, B. L., and Seyed-Yagoobi, J. (1997). Theoretical and experimental study of electrohydrodynamic heat transfer enhancement through wire-plate corona discharge. *Journal of Heat Transfer*, **119**, 604–610.

Pan, Y., and Banerjee, S. (1996). Numerical simulation of particle interactions with wall turbulence. *Physics of Fluids*, **8**, 2733-2755.

Papavassiliou, D. V., and Hanratty, T. J. (1995). The use of Lagrangian methods to describe turbulent transport of heat from a wall. *Industrial and Engineering Chemistry Research*, **34**, 3359–3367.

Perry, A., and Chong, M. S. (1987). A description of eddying motions and flow patterns using critical point concepts. *Annual Review of Fluid Mechanics*, **9**, 125–148.

Reynolds, W. C., and Hussain, F. (1972). The mechanics of an organized wave in turbulent shear flows. Part 3. Theoretical models and comparison with experiments. *Journal of Fluid Mechanics*, **54**, 263–288.

Roth, J. R., Sherman, D. M., and Wilkinson, S. P. (1998). Boundary layer flow control with a one atmosphere uniform glow discharge surface plasma. *AIAA 98-0328, 36th Aerospace Sciences Meeting*, January 12-15, 1998, Reno (NV).

Roth, J. R., Sherman, D. M., and Wilkinson, S. P. (2000). Electrohydrodynamic flow control with a glow-discharge surface plasma. *AIAA Journal*, **38**, 1166-1172.

Schoppa, W., and Hussain, F. (1996). New aspects of vortex dynamics relevant to coherent structures in turbulent flows. In Bonnet, J. P., ed., *Eddy Structure Identification*, Springer-Verlag, Wien, 61–143.

Schoppa, W., and Hussain, F. (1997). Genesis and dynamics of coherent structures in near-wall turbulence. In Panton, R., ed., *Self-sustaining Mechanisms of Wall Turbulence*, Computational Mechanics Publications, 385–422.

Schoppa, W., and Hussain, F. (1998). A large-scale control strategy for drag reduction in turbulent boundary layers. *Physics of Fluids*, **10**, 1049–1051.

Schoppa, W., and Hussain, F. (2000). Coherent structure dynamics in near-wall turbulence. *Fluid Dynamics Research*, **26**, 119–139.

Soldati, A. (1998). Turbulence control and drag reduction by means of large-scale EHD structures. *International Workshop on Electrical Conduction, Convection and Breakdown in Fluids*, Seville (Spain), March 27-28, 1998, 119–124.

Soldati, A. (2000). On the effects of electrohydrodynamic flows and turbulence on aerosol transport and collection in wire-plate electrostatic precipitators. *Journal of Aerosol Science*, **31**, 293–305.

Soldati, A. (2000). Modulation of turbulent boundary layer by EHD flows. *ERCOFTAC Bulletin*, **44**, 50–56.

Soldati, A. (2000). Modulation of turbulent channel flow by large-scale streamwise electrohydrodynamic vortical flows (Submitted for pubblication).

Soldati, A., Andreussi, P., and Banerjee, S. (1993). Direct simulation of turbulent particle transport in electrostatic precipitators. *AIChE Journal*, **39**, 1910–1920.

Soldati, A., and Banerjee, S. (1997). Drag reduction mechanisms in a turbulent Poiseuille flow with superimposed EHD structures. *Bulletin of American Physics Society*, **42**, 2247–2254.

Soldati, A., and Banerjee, S. (1998). Turbulence modification by large scale organized electrohydrodynamic flows. *Physics of Fluids*, **10**, 1742–1756.

Velkoff, H. R., and Godfrey, R. (1979). Low-velocity heat transfer to a flat plate in the presence of a corona discharge in air. *Journal of Heat Transfer*, **101**, 157–163.

Willmarth, W. W., and Lu, S. S. (1972). Structure of the Reynolds stress near the wall. *Journal of Fluid Mechanics*, **55**, 65-92.

Yamamoto, T., and Velkoff, H. R. (1981). Electrohydrodynamics in an electrostatic precipitator. *Journal of Fluid Mechanics*, **9**, 108–122.